

## THRILS – The High-(Redshift+Ionization) Line Search: Program Description & Redshift Catalog

TAYLOR A. HUTCHISON , REBECCA L. LARSON , PABLO ARRABAL HARO , ERINI LAMBRIDES ,  
KATHERINE CHWOROWSKY , GOURAV KHULLAR (गौरव कुल्लर) , KELCEY DAVIS , STEVEN L. FINKELSTEIN ,  
JANE R. RIGBY , GUILLERMO BARRO , NIKKO J. CLERI , DALE KOCEVSKI , JACQUELINE ANTWI-DANSO ,  
MIC BAGLEY , DANIELLE A. BERG , VOLKER BROMM , OSCAR CHAVEZ ORTIZ , JOHN CHISHOLM ,  
SADIE C. COFFIN , M. C. COOPER , OLIVIA COOPER , ISA G. COX , MARK DICKINSON , HARRY FERGUSON ,  
MAXIMILIEN FRANCO , JONATHAN P. GARDNER , ANANYA GANAPATHY , NORMAN GROGIN ,  
MICHAELA HIRSCHMANN , MARC HUERTAS-COMPANY , INTAE JUNG , JEYHAN S. KARTALTEPE ,  
ANTON M. KOEKEMOER , RAY A. LUCAS , ELIZABETH MCGRATH , ALEXA M. MORALES , GRACE M. OLIVIER ,  
CASEY PAPOVICH , PABLO G. PÉREZ-GONZÁLEZ , NOR PIRZKAL , RACHEL S. SOMERVILLE ,  
ANTHONY J. TAYLOR , JONATHAN R. TRUMP , BRITTANY VANDERHOOF , BENJAMIN WEINER , BRIAN WELCH ,  
L. Y. AARON YUNG  AND JORGE A. ZAVALA 

THE THRILS COLLABORATION

### Abstract

To date, many spectroscopic confirmations of  $z > 7$  galaxies have been obtained using *JWST*/NIRSpec prism observations, with most of their physical properties inferred from these observations and corresponding imaging. What is needed are higher-resolution spectra at deeper depths to study these sources in detail. We present The High-(Redshift+Ionization) Line Search (THRILS) program: deep ( $>8$  hr) observations in two pointings of *JWST*/NIRSpec G395M spectroscopy to 1) probe high ionization spectral features in  $z > 8$  galaxies that are indicative of top-heavy initial mass functions or growing massive black holes, 2) search for accreting supermassive black holes in typical galaxies at  $z \sim 4-9$  through broad Balmer line emission, and 3) probe the stellar-mass growth histories of massive galaxies. We include spectroscopic redshift measurements for 89 sources from the THRILS data, as well as a detection threshold for the full and  $\sim$ half depth integration times of the program.

### 1. INTRODUCTION

Over the past few years, galaxy evolution has witnessed an explosion of exciting science from *JWST* (J. P. Gardner et al. 2023), with many discoveries shedding light on previously unreachable observations of early epochs. In the myriad discoveries from the first few years of *JWST*'s mission, three results stand out for their unexpected nature and their potential to illuminate the earliest phases of galaxy formation (e.g., V. Bromm & N. Yoshida 2011).

Initial results from early *JWST* imaging detected the presence of galaxies at  $z > 9$  (e.g., N. J. Adams et al. 2022; S. L. Finkelstein et al. 2022a; H. Atek et al. 2023). While finding such galaxies was one of the primary science goals of *JWST*, the high abundance and the existence of very bright sources out to photometric redshifts of 17 were unexpected (C. T. Donnan et al. 2022; Y.

Harikane et al. 2022). While the lack of empirical constraints prior to *JWST* meant that model predictions for the volume density of such sources spanned orders of magnitude, the observations lie at the very high end of these predictions (e.g. S. L. Finkelstein et al. 2022b, 2024; Y. Harikane et al. 2022; P. G. Pérez-González et al. 2023, 2025b). Since launch, *JWST* spectroscopy has produced a high success rate for photometric selection of high-redshift sources and confirms the overabundance of high-redshift galaxies (e.g. E. Curtis-Lake et al. 2023; S. Fujimoto et al. 2023; P. Arrabal Haro et al. 2023a; M. Tang et al. 2024, 2025b; R. P. Naidu et al. 2025a, and many others). Among the more likely physical mechanisms missing from the previous lower model predictions is a top-heavy initial mass function (IMF) – proposed to become dominant at very low metallicities (where fragmentation into “smaller” stars would be less efficient, e.g., A. Venditti et al. 2023), as expected for galaxies at such early times (e.g., R. Schneider et al. 2002; V. Bromm & A. Loeb 2003; E. R. Cueto et al.

2024). This possible mechanism is empirically testable via the detection of high ionization emission lines such as singly-ionized Helium (He II  $\lambda 1640$ , He II  $\lambda 4687$ ; e.g., V. Bromm et al. 2001b; D. Schaerer 2003; G. M. Olivier et al. 2022; R. Maiolino et al. 2023; K. Nakajima & R. Maiolino 2022; E. Zackrisson et al. 2024) and/or quadruply-ionized Neon ([Ne V]  $\lambda 3426$ ; e.g., N. J. Cleri et al. 2023a,b; J. Chisholm et al. 2024).

Additionally, early *JWST* programs uncovered a surprising population of peculiar growing super-massive black holes (SMBHs, hereinafter active galactic nuclei; AGN) selected by broadened Balmer emission indicative of  $>1000 \text{ km s}^{-1}$  moving gas (broad-line or BLAGN; e.g., R. Maiolino et al. 2023; Y. Harikane et al. 2023; D. Kocevski et al. 2023; R. L. Larson et al. 2023; J. Matthee et al. 2024). From X-ray to Radio, this population appears to lack most multi-wavelength AGN signatures; their estimated number densities and black hole masses challenge expectations built on pre-*JWST* predictions (T. T. Ananna et al. 2024; M. Yue et al. 2024; A. Lupi et al. 2024; E. Lambrides et al. 2024; A. J. Gloude-mans et al. 2025; C. C. Williams et al. 2024; B. Wang et al. 2025a; H. B. Akins et al. 2025; K. Ronayne et al. 2025). This includes a subset of sources, dubbed “Little Red Dots” or LRDs, which have launched intensive debate surrounding their formation and fate in attempting to physically motivate their observed “v-shaped” spectral energy distributions (SEDs) complete with a rest-frame UV excess alongside red *JWST*/NIRCam colors ( $m_{277} - m_{444} > 1.5 \text{ mag}$ ; G. Barro et al. 2024a; L. J. Furtak et al. 2024; J. Matthee et al. 2024; J. E. Greene et al. 2023; V. Kokorev et al. 2023; D. Kocevski et al. 2023; V. Kokorev et al. 2024a,b; P. G. Pérez-González et al. 2024a; H. B. Akins et al. 2025). Some attempts to explain the discrepancy between canonical AGN characteristics and these new sources are centered on 1) variance in the dust properties (i.e., temperatures, grain sizes; C. M. Casey et al. 2024; D. J. Setton et al. 2025), 2) the possibility for more extreme accretion (e.g., A. King 2024; F. Pacucci & R. Narayan 2024; M. Yue et al. 2024; E. Lambrides et al. 2024; P. Madau & F. Haardt 2024a; A. Lupi et al. 2024), or 3) or extremely compact star formation de-emphasizing the need for an AGN at all (e.g., P. G. Pérez-González et al. 2024a; C. C. Williams et al. 2024; H. B. Akins et al. 2025; G. C. K. Leung et al. 2024; P. Madau & F. Haardt 2024b; B. Wang et al. 2025a; K. E. Whalen et al. 2025). The majority of spectroscopically-confirmed *JWST* BLAGN samples (including LRDs) are from relatively shallow observations ( $<3 \text{ hr}$ , in *JWST* cycles 1 & 2), targeted with lower resolution *JWST*/NIRSpec prism ( $R \sim 100$ ) spectroscopy. While these essential early surveys were

critical for confirming photometrically-selected samples, breaking the degeneracy between competing interpretations of these sources requires deeper and higher-resolution data. Specifically, reaching depths that allow for robust searches of faint ionization lines ( $F_{line} \simeq 0.1 \times F_{[OIII]}$ ) will aid in understanding the complete ionization state of the hot ionized gas, and higher-resolution ( $R \gtrsim 1000$ ) will enable better disentangling of complex blended line systems such as what has been observed in the Balmer series in BLAGN with *JWST*.

Another curious result from early *JWST* papers was the discovery of galaxies with very large presumed stellar masses ( $\log(M/M_{\odot}) > 10$ ) at redshifts up to  $z \sim 9$  (I. Labbe et al. 2022, e.g.). If these galaxies were as massive and abundant as initially reported, they would directly challenge predictions from  $\Lambda$ CDM (e.g., see early discussion in M. Boylan-Kolchin 2022). Updated results from multiple studies indicate the masses are likely somewhat lower (e.g., D. Kocevski et al. 2023; J. E. Greene et al. 2023; K. Chworowsky et al. 2023; G. C. K. Leung et al. 2024; P. G. Pérez-González et al. 2024a). With a modest area coverage of  $\sim 90 \text{ arcmin}^2$ , the CEERS survey (S. L. Finkelstein et al. 2024) appears to contain  $\sim 50$  such systems at  $z > 4$ , with  $\sim 20$  at  $z > 6$ , some even appearing to have ceased their star-forming activity (e.g., A. C. Carnall et al. 2023a; T. J. Looser et al. 2023). While growing to  $\log(M/M_{\odot}) > 10$  in  $<1 \text{ Gyr}$  is not impossible, it is not predicted by current models at the observed abundance (F. Valentino et al. 2023; A. Weibel et al. 2025; T. Wang et al. 2025). Such galaxies must form their stars at a remarkably rapid rate (e.g., K. Glazebrook et al. 2024; Euclid Collaboration et al. 2025). Those that are already quiescent at high redshifts must have shut down their star formation just as rapidly (e.g., A. C. Carnall et al. 2023b, 2024). The best path to understanding the formation of these massive galaxies is to reveal their star-forming histories (SFHs; e.g., K. Chworowsky et al. 2023; A. C. Carnall et al. 2024; K. Glazebrook et al. 2024; M. Xiao et al. 2024, Khullar et al., in prep; also see J. Matthee 2025 for a review).

Addressing these three questions — 1) the presence of a top-heavy IMF in the early galaxies, 2) the nature of the gas surrounding high- $z$  BLAGN and LRDs, and 3) the SFHs of massive early galaxies — requires deep, rest-frame optical spectroscopy of targeted high-redshift sources. The High-[Redshift+Ionization] Line Search (THRILS; PIs T. Hutchison & R. Larson, GO-5507) program obtained deep ( $>8 \text{ hr}$ ) *JWST*/NIRSpec spectroscopy with the G395M medium-resolution ( $R \sim 1000$ ) grating for 184 sources in the EGS field (with the majority of these sources previously photometrically discov-

ered in the Cosmic Evolution Early Release Science, or CEERS, Survey *JWST*/NIRCam imaging, M. B. Bagley et al. 2022; S. L. Finkelstein et al. 2025). In this paper, we present the THRILS survey design (§2), describe the observations and data reduction (§3), and publish a spectroscopic redshift catalog including a list of non-detections (§4). Finally, we detail an overview of the THRILS program science goals (§5). In this work, we assume a standard flat cold dark matter universe with a cosmological constant ( $\Lambda$ CDM), corresponding to the nine-year Wilkinson Microwave Anisotropy Probe (WMAP9, G. Hinshaw et al. 2013).

## 2. SURVEY DESIGN

The EGS / CEERS (S. L. Finkelstein et al. 2025) field has been heavily studied by teams around the globe, with growing excitement regarding spectroscopic detections of galaxy overdensities from galaxies at various epochs in the early Universe ( $z = 4.9, 7.8, 8.7$ ; e.g., R. L. Larson et al. 2022a; M. Tang et al. 2023; L. Whitler et al. 2022; V. Tilvi et al. 2020; I. Jung et al. 2022; P. Arrabal Haro et al. 2023b; L. Whitler et al. 2025). Such galaxy overdensities highlight the thrilling nature of the CEERS field and its scientific potential to detect even fainter sources in these same early epochs. Additionally, the deep and extensive multi-wavelength photometry of the broader legacy EGS field enables high-fidelity photometric redshifts, and the plethora of public spectroscopic data verifies many of our photometric selections.

### 2.1. Ancillary Data Catalog Creation

The primary science goals of THRILS require photometric selection of galaxies across  $4 \lesssim z \lesssim 10$ . To do this, we created a combined catalog for the EGS field using the public CEERS NIRCam and MIRI imaging (S. L. Finkelstein et al. 2025; M. B. Bagley et al. 2022; G. Yang et al. 2023), and the CEERS NIRSpec and NIRCam WFSS spectroscopy (N. Pirzkal et al. 2017; Arrabal Haro et al. in prep). Additionally, for legacy ancillary data we include products from CANDELS (N. A. Grogin et al. 2011; A. M. Koekemoer et al. 2011), specifically the public CANDELS *HST*+*Spitzer* catalog (M. Stefanon et al. 2017) and the CANDELS EGS catalog from S. L. Finkelstein et al. (2022c, hereafter F22). We also use external *JWST* products from the Dawn *JWST* Archive<sup>1</sup> (DJA; A. de Graaff et al. 2024; K. E. Heintz et al. 2024) for recent spectroscopic redshifts, as well as a compilation of ground-based spectroscopic programs (R. L. Sanders et al. 2021; R. L. Larson et al. 2022a; I. Jung et al. 2018; S. M. Urbano Stawinski et al. 2024).

For the CEERS imaging, we used the UNICORN photometric catalog (S. Finkelstein et al., in prep.), which places particular emphasis on measuring accurate colors and total fluxes and includes photometric redshifts with improved templates (R. L. Larson et al. 2022b).

To create a comprehensive combined catalog, we match all source catalogs to within 0.5" using TOPCAT (M. Taylor 2011). This yielded 169,011 unique sources across all of EGS. We then created several columns for our use: RA, DEC, a magnitude in three bands (H, 3.6  $\mu\text{m}$ , and 4.5  $\mu\text{m}$ ), a photometric redshift ( $z_{\text{phot}}$ ), and a spectroscopic redshift ( $z_{\text{spec}}$ ). We also created columns labeled  $z_{\text{phot}}$  vetted and  $z_{\text{spec}}$  vetted for each source. We populated these columns with values in order of most recent or highest resolution. For the RA and DEC columns, we use the coordinates from NIRCam where available (including the WFSS data), then from NIRSpec, followed by the CANDELS *HST* coordinates for those sources that were not observed with NIRCam or NIRSpec (corrected to match the more accurate, Gaia-anchored astrometric reference frame for the CEERS NIRCam image mosaics), and finally the MIRI coordinates for the  $\sim 840$  sources that were only detected in MIRI imaging.

To fill out the magnitude columns, we chose three representative bands: H, 3.6 $\mu\text{m}$ , and 4.5 $\mu\text{m}$ , as there are observations at these wavelengths from both *JWST* and *HST* or *Spitzer* – the latter two of which overlap with the NIRSpec G395M filter. For the H-band magnitudes ( $m_H$ ), we use the measured flux in the *JWST*/NIRCam F150W filter where observed and the *HST*/WFC3 F160W for those outside of the NIRCam coverage. For any sources that do not have an observed magnitude in either of these bands (i.e., those that are only MIRI detected), we use a value of  $-1$  in this column. We follow a similar procedure for the other two magnitude bins ( $m_{3.6}$  and  $m_{4.5}$ ), using the *JWST*/NIRCam F356W (including from the CEERS WFSS data) or F444W, where observed, or the *Spitzer* Ch1 or Ch2 when outside of the *JWST* coverage. Again, for any sources that do not have an observation in one of these bands, we assign a  $-1$  value to that column.

The photometric redshift column ( $z_{\text{phot}}$ ) is populated by first using the redshift values based upon the CEERS NIRCam observations (I. G. Cox et al. 2025), then using those from the *HST*+*Spitzer* CANDELS catalog (D. Kodra et al. 2023), and finally those from the CANDELS EGS catalog (F22). Each of these catalogs has a ranking value for its photometric redshifts, which we use to assess the reliability of the measurements and assign a grade to the  $z_{\text{phot}}$  vetted column. Sources from the NIRCam and the F22 catalog were vetted for photometric

<sup>1</sup> <https://dawn-cph.github.io/dja/spectroscopy/nirspec/>

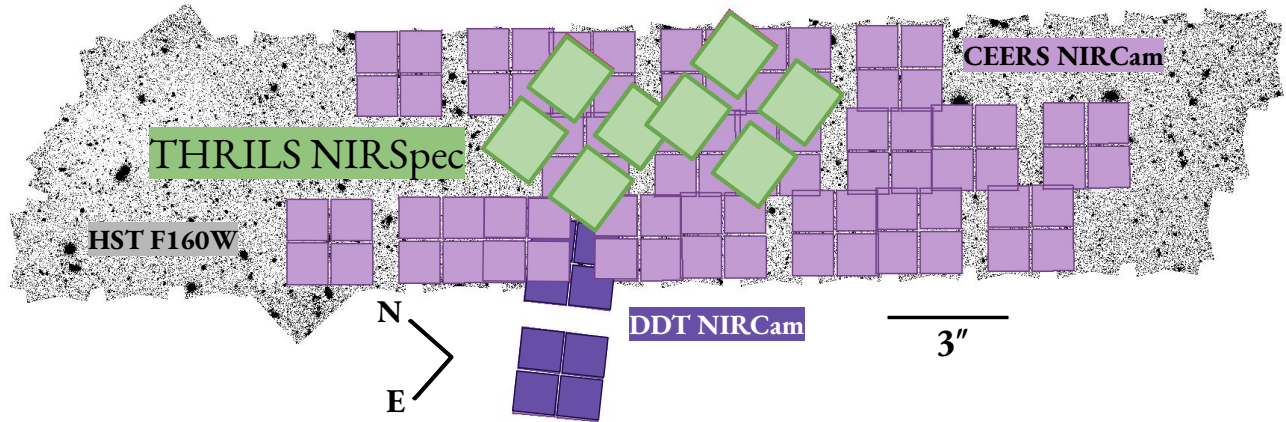


**Figure 1.** The two THRILS NIRSpec pointings (green) overlaid on the *HST*/F160W mosaic image from CANDELS (N. A. Grogin et al. 2011; A. M. Koekemoer et al. 2011), with the CEERS NIRCcam coverage outlined in purple (M. B. Bagley et al. 2022; S. L. Finkelstein et al. 2025). The parallel NIRCcam imaging from NIRSpec DDT program 2750 (P. Arrabal Haro et al. 2023b) is shown in dark purple.

redshifts by meeting a set of criteria, namely requiring detection significance in at least two photometric bands and reasonably well-constrained photometric redshifts. The CANDELS catalog values were taken at face value unless they had bad flags, such as those near stars or at the edges of the images (M. Stefanon et al. 2017). Photometric redshifts are vetted by applying a value of 2 if the  $z_{phot}$  is believed, a 1 if it is likely but uncertain, a 0 if it is NOT believed, and a  $-1$  if it is not vetted. This means that sources with a value in the  $z_{phot}$  column and a 2 in the  $z_{phot}$  vetted column are likely robust measurements; however, those with a 0 in the vetted column should not be used in any analysis.

The spectroscopic redshift column ( $z_{spec}$ ) first uses the value in the CEERS spectroscopic redshift catalog (Arrabal Haro et al. in prep), then the value from the DJA, followed by the value from the CANDELS catalog, followed by the ground-based redshifts from Keck/MOSFIRE (MOSDEF; R. L. Sanders et al. 2021) and DEIMOS (S. M. Urbano Stawinski et al. 2024). Each of these catalogs assigns a grade to the believability of the redshift measurement, and we use those grades to determine a value for our vetting. Spectroscopic redshifts are vetted by applying a value of 2 if the  $z_{spec}$  is believed, a 1 if it is likely but uncertain, a 0 if it is NOT believed, and a  $-1$  if it is not vetted. For example, those sources in the DJA that have a grade of 3 (flagged by DJA as robust) are assigned a  $z_{spec}$  vetted value of 2, but those that have a DJA grade of 0 (flagged by DJA as a data quality issue) or 1 (flagged by DJA as having no features) are assigned a vetted value of 0 and not used in the target selection.

## 2.2. Target Selection

We selected targets for our observations based upon the three main science goals of the program: 1) higher-redshift ( $z > 7$ ) and high ionization lines, 2) high-redshift AGN ( $z > 4$ ), and 3) high-redshift massive galaxies ( $z > 4$ ), as described below.

We selected sources for Science Case 1 (higher-redshift and high-ionization galaxies, see §5.1) using several methods. To identify sources that met both criteria, we selected sources with spectroscopic or photometric redshifts at  $z > 6$ , which were expected to have higher ionization based on photometric color selection techniques (potentially powered by recent starbursts). We summarize the method here: in brief, we used several photoionization models of young ( $< 50$  Myr), sub-Solar-metallicity star-forming galaxies spanning a broad range of ionization. We generated the NIRCcam colors F356W–F444W as the initial color cut, selecting photometric redshifts for which strong lines, driven by very high ionization, dominate the color. Secondary selections were made using NIRCcam colors F277W–F356W and F410M–F470N, following similar criteria. The final rankings were made from a combination of the primary and secondary color selections.

Separately, to build a larger sample of general high-redshift sources, we followed the selection of S. L. Finkelstein et al. (2022a), who selected sources at  $z > 8$  in the CEERS NIRCcam imaging (M. B. Bagley et al. 2022) and visually vetted them as robust high-redshift candidates. Finally, for Science Case 1, we selected extreme emission-line galaxies (EELGs) in the CEERS imaging using the method described by K. Davis et al. (2024).

Our parent AGN sample for Science Case 2 (see §5.2) was compiled from several previously published catalogs spanning X-ray to radio wavelengths (K. Nandra

et al. 2015; S. Q. Park et al. 2010; R. J. Ivison et al. 2007), as well as recent *JWST* MIRI imaging observations (B. E. Backhaus et al. 2025). We also included the broad-line AGN (BLAGN) from A. J. Taylor et al. (2025a), which were identified in the CEERS and Red Unknowns: Bright Infrared Extragalactic Survey (RUBIES, GO-4233, PIs: A. de Graaff & G. Brammer; A. de Graaff et al. 2025). We also include LRDs from D. D. Kocevski et al. (2022) and G. Barro et al. (2024b).

The massive galaxies for Science Case 3 (see §5.3) were selected by running Dense Basis (K. G. Iyer et al. 2021) on the CEERS NIRCcam imaging to identify sources at  $z > 4$  with stellar masses  $\log(M_*/M_\odot) > 10$ . We required that 95% of the posterior on stellar mass lie at  $\log(M_*/M_\odot) > 10$ , ensuring that our targets have a high likelihood of being massive galaxies. We then performed visual vetting on each candidate galaxy to remove spurious detections and sources with contaminated photometry, such as sources affected by blending with nearby objects, diffraction spikes, or NIRCcam imaging artifacts. This selection process is similar to that of K. Chworowsky et al. (2024).

### 2.3. Weighting for MPT

Using our combined catalog, we then need to assign weights for the MSA Planning Tool (MPT) to optimize our observations. We begin by applying a base weighting scheme that strongly favors higher redshifts and quickly downgrades sources that become too faint to be detected, regardless of their potential interest. The simplified formula would be:

$$\log(W) = \min(5, z/2)$$

if  $\min(m) \leq m_{threshold}$ , and

$$\log(W) = \min(5, z/2 + 2.5 * [m_{threshold} - \min(m)])$$

if  $\min(m) > m_{threshold}$ ,

where  $W$  is the MSA weight,  $z$  is the best redshift available for the object ( $z_{spec}$  when available, otherwise  $z_{phot}$ ),  $m_{threshold}$  is the estimated detection depth of the program (here we use 28 ABmag), and  $\min(m)$  is the magnitude in the brightest band ( $m_{3.6}$  or  $m_{4.5}$ ). We down-weight sources with bad-pixel flags in the F22 catalog and those with star flags in the CANDELS catalog (M. Stefanon et al. 2017). To mitigate small sources at the edges of images that were receiving the maximum base MPT weights, we down-weighted all sources that did not have a vetted  $z_{phot} > 2$  or a vetted  $z_{spec} > 1$ .

Using the MSA Planning Tool in the APT, we determine field centers by developing a source prioritization scheme, where the highest-priority sources are the

spectroscopically confirmed ( $z > 8$ ) sources, the brightest spectroscopically confirmed LRD, and the massive ( $z > 4$ ) galaxies. Our other primary targets are those described in our target selection section above and are assigned the next-highest tier of priority. Lower priorities are assigned to progressively lower-redshift and fainter sources. We further split our two pointings into two observing sequences each, in which we swapped out observed filler sources halfway through the observations ( $\sim 4$  hr per pointing) for new filler sources.

## 3. DATA

### 3.1. Observations

We used 3-shutter slitlets and a 3-shutter nodding pattern in two different configurations per pointing, utilizing the NRSIRS2 rapid readout pattern for NIRSpec (T. Böker et al. 2023). Our two pointings had slightly different total exposure times as the higher-priority and higher-redshift sources were predominantly located in Pointing 1 (Figure 1, left THRILS pointing). We used 18 groups per integration and 4 integrations per exposure in Pointing 1, thus setting the time per individual exposure to 5310.356 s. In Pointing 2 (Figure 1, right THRILS pointing), we used 17 groups per integration and 4 integrations per exposure, resulting in a single exposure time of 5018.5781 s. We observed 2 configurations per pointing, with 3 exposures per configuration. In our second configuration, we swapped out filler targets where possible but kept the primary targets in shutters for the full observation time. This yields a total exposure time of 8.85 hr (8.36 hr) for our primary sources in Pointing 1 (Pointing 2). The center RA & Dec coordinates are (214.9578413 deg, +52.9193425 deg) for Pointing 1 and (214.8699359 deg, +52.8724952 deg) for Pointing 2. The two pointings were at slightly different position angles (PAs) with Pointing 1 at 3.9473 deg and Pointing 2 at 4.0115 deg. While the FOVs of the two NIRSpec pointings overlap in a small corner of both detectors, we did not place any sources in that region for either pointing due to mask optimization. Pointing 1 had 98 total targets, with 26 primary sources, 57 filler targets, and 16 contaminating sources. Pointing 2 covered 86 targets in total, with 33 primary sources, 44 filler targets, and 12 contaminants. In total, we observed 184 sources, of which 59 were from our three primary science cases and received the full exposure time. We note that some ( $\sim 24$ ) of the sources observed in THRILS had previous spectroscopic measurements, which we discuss in §4.

## 3.2. Data Reduction

The THRILS NIRSpec data were reduced using the *JWST* Calibration Pipeline version 1.17.1 (H. Bushouse et al. 2022, DOI:10.5281/zenodo.7429939) with CRDS context `jwst_1350.pmap`. The processing is based on standard pipeline parameters, with several modifications for specific steps. Here we give some relevant specifics, including deviations from standard processing:

*FFLAT Reference Files:* We use modified FFLAT reference files. The current reference file for the FFLAT (Fore optics FLAT-field) contains very large values in the error extension, resulting from the observed calibration star not matching the expected model during commissioning observations. Only some pixels (wavelengths) have these very large error values, which then propagate to produce unreasonably large flux errors in the reduced spectra. As a result, we mask out the entire error array from the FFLAT files for our reductions.

*Stuck-Closed Shutters:* Unexpectedly stuck-closed shutters are detected through the identification of missing sky emission in the background-unsubtracted 2D spectra. The MSA metafiles are modified to account for these failed closed shutters. The dithering nods in which the target is behind a failed closed shutter are omitted when combining the dithers to generate the final spectra. This is reflected in the measured total exposure time per source in the catalog (§4). The MSA metafiles are also modified to implement the correct extraction at the expected location for known companion sources.

*Point Sources:* The pipeline was instructed to treat all targets as point sources (SRCTYPE = “POINT”) – such that no BARSHADOW correction was applied, and the 1D spectra are in units of flux density rather than surface brightness. The default pipeline pathloss correction was employed, and the flux calibration used the default reference files for the adopted CRDS context.

*Optimized Extraction:* To obtain 1D spectra from each of these 2D spectra, we then use an optimal extraction (K. Horne 1986), determined by spatially collapsing the 2D spectrum and fitting the spatial profile of the source with a Gaussian. We applied median filtering to remove any bright artifacts before collapsing the 2D spectrum. This also ensures that any potential contaminating objects are masked from the extraction profile for each source. The resulting spatial profile is then used as the weight for optimal 2D-to-1D extraction for each source, ensuring that the shape and extent of each source are correctly accounted for in the extraction weights.

## 4. REDSHIFT CATALOG

Here, we provide a spectroscopic redshift catalog for all sources with detections in the THRILS survey. In-

Table 1. The Abbreviated THRILS Survey Redshift Catalog

THRILS ID <sub>MPT</sub>	Coordinates			THRILS			Magnitudes			Prior Redshifts	
	RA	DEC	$z_{spec}$	Grade	ExpTime [s]	Category	H	3.60	4.50	$z_{phot}$	$z_{spec}$
102659	214.943146	52.94244	11.41	2	31862	Primary	28.4±0.1	27.95±0.04	27.68±0.04	11.6 <sup>10.0</sup> <sub>10.0</sub>	11.42 <sup>a</sup>
117286	214.977181	52.926547	9.0307	1	15931	Filler	28.6±0.1	28.78±0.09	29.0±0.2	9.0 <sup>9.9</sup> <sub>1.4</sub>	-1
92641	214.823994	52.884186	8.93	1	15056	Filler	28.78±0.06	28.86±0.04	28.9±0.05	8.0 <sup>8.6</sup> <sub>1.8</sub>	-1
97442	214.838696	52.882226	8.929	3	30111	Primary	29.2±0.1	28.96±0.06	28.28±0.03	9.0 <sup>10.0</sup> <sub>8.7</sub>	-1
37717	214.938864	52.911749	8.7578	3	31862	Primary	26.48±0.02	26.76±0.01	26.24±0.009	9.0 <sup>9.0</sup> <sub>8.8</sub>	8.768 <sup>b</sup>
19512	214.967531	52.932951	8.7146	3	31862	Primary	26.1±0.02	26.46±0.01	26.1±0.008	9.0 <sup>8.8</sup> <sub>8.8</sub>	8.717 <sup>b</sup>

NOTE—Abbreviated version of the THRILS Redshift Catalog. The full version of this table is in the Appendix, and a machine-readable version is provided with the publication of this work. Description of Columns: 1) ID in the THRILS MPT, 2-3) Coordinates, 4-5) Measured  $z_{spec}$  in THRILS and grade for this redshift as described in §4.1, 6-7) Exposure time and target category for the source as described in §2.2, 8-10) Magnitude of the source in 3 representative bands as described in §2.1, 11-12) Prior measurements of  $z_{phot}$  and  $z_{spec}$  from ancillary data as described in §2.1.

<sup>a</sup> *JWST* DDT 2750 (P. Arrabal Haro et al. 2023a).

<sup>b</sup> CEERS (Arrabal Haro et al. in prep).

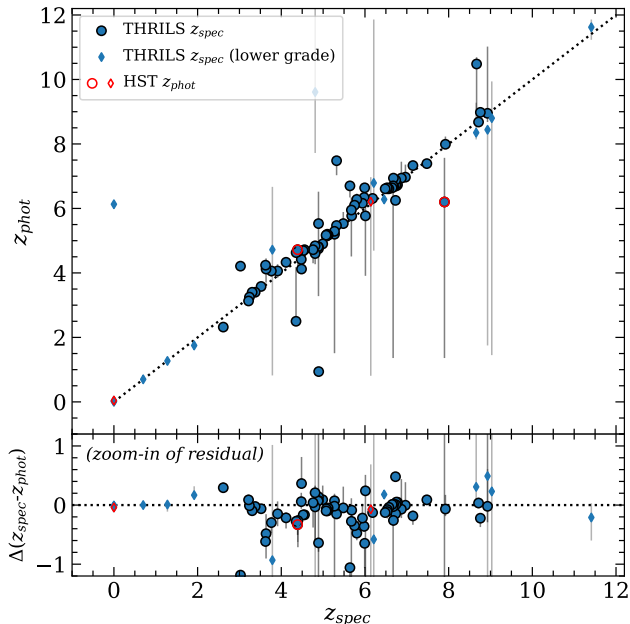


**Figure 2. Spectroscopic vs photometric redshift.** (top)  $z_{spec}$  vs  $z_{phot}$  for all 89 sources with measured redshifts in THRILS. The robust redshift measurements (grade = 3) are shown as blue circles, while the lower confidence measurements (grade < 3) are shown as diamonds. We annotate all  $z_{phot}$  derived from *HST*-only data with red borders. (bottom) Residual of  $z_{spec} - z_{phot}$ , zoomed into sources around zero for clarity.

cluded columns are the MPT ID from THRILS, RA and Dec of the source, a measured spectroscopic redshift ( $z_{spec}$ ), a redshift grade, exposure time on source, target category (Primary, Filler, or Contaminant), magnitudes in 3 bands ( $m_H$ ,  $m_{3.6}$ , and  $m_{4.5}$ ), and prior photometric ( $z_{phot}$ ) and spectroscopic ( $z_{spec}$ ) redshift information as described above in §2.1. Sources that have *HST*-only derived  $z_{phot}$  measurements, as they lie outside the CEERS NIRCcam coverage, are marked with an asterisk (\*). The first six rows are shown in Table 1 as an example, and the whole catalog is provided in the Appendix (Table 3). A machine-readable table is also provided with the publication of this paper.

#### 4.1. Redshift Measurements

The redshifts were measured using an automated line-finding software (R. L. Larson et al. 2018, 2023) designed to fit and identify emission-line features. The code uses a photometric redshift prior to determine the expected brightest line in the spectrum (i.e., [O III]  $\lambda 5008$  or H $\alpha$   $\lambda 6564$ ), and fits the redshift to the line center. At least two team members visually vetted all redshifts published in this work for accuracy. For those with a single detected emission line, the photo- $z$  was used to obtain best-

guess redshifts. When line identification is ambiguous, the redshift grade is lowered (see below). For the few sources with detected emission that could not be identified, we assigned a  $z_{spec} = -2$ . For sources with detected continuum but no discernible emission with which to measure a redshift, we assigned a  $z_{spec} = -3$ .

The spectroscopic redshifts are graded as follows: 3 denotes a robust spectroscopic redshift, with multiple or distinct emission lines detected. A grade of 2 is assigned when faint emission lines are detected but are likely to be correctly identified, and thus the redshift is considered secure. A grade of 1 is for those with tentative line detections, but which are in agreement with prior photometric or spectroscopic redshift measurements, or those with one line detected, and an approximation is made for the redshift. A grade of 0 is assigned to sources with detected lines that cannot be identified ( $z_{spec} = -2$ ) or with detected continuum but no emission lines detected ( $z_{spec} = -3$ ). Finally, there were a small number of sources that we suspect are stars or brown dwarfs and were thus assigned  $z_{spec} = 0$  with a grade of 1.

In total, we publish spectroscopic redshift measurements for 89 sources in THRILS and an additional 13 sources that show emission lines or continuum but for which we could not discern a likely redshift. In Figure 2 we show the measured  $z_{spec}$  vs  $z_{phot}$  for these sources. For clarity, we distinguish between those with robust measurements (grade = 3, circles) and those with lower-confidence redshifts (grade < 3, diamonds). We also highlight sources with no *JWST*/NIRCcam imaging (and thus only with a  $z_{phot}$  from *HST*) with red outlines. In the bottom panel of Figure 2, we show a zoom in on the residuals around zero, highlighting that most of our photometric redshifts are in good agreement with the measured spectroscopic redshifts.

We present an abbreviated view of the catalog of these sources in Table 1 and provide the full redshift catalog in Table 3 in the Appendix. Of the 89 sources with spectroscopic redshifts derived from the THRILS program, only 24 had previous spectroscopic measurements (primarily from NIRSpc/MSA prism observations). We note any previous spectroscopic redshift measurements in the final column of both Tables 1 & 3, with table footnotes denoting the reference catalogs or publications from which the previous measurements were obtained.

#### 4.2. Discussion of Non-Detections

In the THRILS data, 81 sources were not detected (i.e., those with no detectable signal), of which only 2 were primary science targets, and only 6 had the complete >8 hr exposure time depth. A majority of the non-detected sources were faint filler targets and/or con-

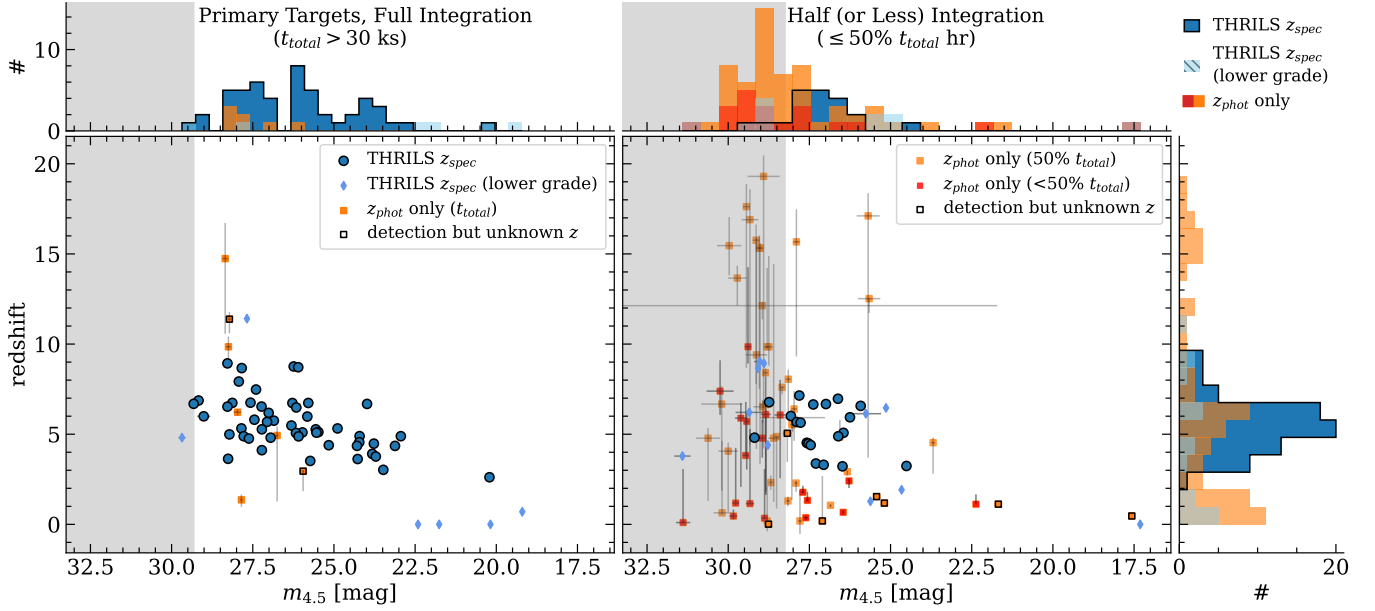


**Figure 3. Detections and magnitude depths.** Plot of the source magnitude at  $4.5 \mu\text{m}$  from *JWST*/NIRCam F444W (or *Spitzer* Ch2 when not observed with *JWST*) vs redshift for the THRILS survey. (*left*) The THRILS primary science targets, with full integration time for each pointing ( $>30$  ks). The THRILS spectroscopic redshifts ( $z_{\text{spec}}$ ) are shown in blue, with high confidence (circles, grade = 3) and lower confidence (diamonds, grade = 1–2) redshifts. For the primary targets that yielded non-detections (orange squares), we use their photometric redshift ( $z_{\text{phot}}$ ) as the displayed redshift. (*right*) The THRILS filler targets or contaminating sources, which had half the integration time (or less) per pointing. The THRILS spectroscopic redshifts are again shown in blue. The non-detected sources are separated into half integration (orange,  $\sim 15$  ks; three dithers) and less than half (red,  $<12$  ks; one or two dithers only). The grey shaded regions show the NIRSpec detection threshold for non-EELGs in both panels, highlighting the depth achieved at both exposure times and advocating for more deep NIRSpec programs.

**Table 2.** Abbreviated Non-Detections from the THRILS Survey

THRILS ID <sub>MPT</sub>	Coordinates		THRILS		Magnitudes			Prior Redshifts	
	RA	DEC	ExpTime [s]	Category	H	3.60	4.50	$z_{\text{phot}}$	$z_{\text{spec}}$
127239	214.85961	52.858029	15056	Filler	-1	-1	-1	-1	6.0611 <sup>a</sup>
136697	215.003204	52.896604	15931	Filler	23.5 $\pm$ 0.003	-1	-1	5.0 <sup>5.8*</sup> <sub>3.4</sub>	-1
139799	214.948036	52.926073	10621	Contaminant	25.7 $\pm$ 0.07	-1	-1	2.0 <sup>8.0*</sup> <sub>1.4</sub>	-1
160204	214.841267	52.891728	15056	Filler	27.17 $\pm$ 0.07	-1	-1	5.0 <sup>5.4*</sup> <sub>2.5</sub>	-1
139366	214.9154	52.904181	15931	Filler	27.5 $\pm$ 0.1	-1	-1	10.5 <sup>10.0*</sup> <sub>3.2</sub>	-1
160727	214.913099	52.941113	15931	Filler	27.7 $\pm$ 0.1	-1	-1	3.0 <sup>10.0*</sup> <sub>2.2</sub>	-1

NOTE—Abbreviated version of the table of non-detections in the THRILS data sorted in order of brightness. We list the full non-detection table in the Appendix Table 2. Description of Columns: 1) ID in the THRILS MPT, 2-3) Coordinates, 4-5) Exposure time and target category for the source as described in §2.2, 6-8) Magnitude of the source in 3 representative bands as described in §2.1, 9-10) Prior measurements of  $z_{\text{phot}}$  and  $z_{\text{spec}}$  from ancillary data as described in §2.1.

\* Sources with  $z_{\text{phot}}$  values from *HST* only, they do not have *JWST*/NIRCam coverage.

<sup>a</sup> DJA (A. de Graaff et al. 2024; K. E. Heintz et al. 2024).

taminating sources that received  $\leq 50\%$  of the program’s full exposure time. The abbreviated view of the non-detected source list is shown in Table 2, and we include the full non-detection catalog in Table 4 in the Appendix. The format follows the same as that of the redshift catalog in §4, however without a redshift measurement or grade. The non-detected sources are sorted in order of brightness in descending wavelength order, with the brightest first. Sources that either lack a detection or are not observed in a specific photometric band are marked with a  $-1$  in that column, and we include these sources at the top of the catalog.

The detection limits of our program are shown in Figure 3, with spectroscopically detected and non-detected ( $z_{phot}$  only) THRILS sources vs  $4.5\mu\text{m}$  magnitude ( $m_{4.5}$ ). The left panel includes all sources at full depth for each pointing ( $>30\text{ks}$  or  $> 8$  hr), with the robust THRILS redshifts (grade = 3) shown as blue circles and the lower-confidence THRILS redshifts (grade = 1–2) as light blue diamonds. The right panel shows sources at half depth or less, with sources that were changed out after 4 hr in each pointing (orange,  $\sim 15\text{ks}$ ) or sources that were contaminants, appearing in only one or two dithers (red,  $\leq 12\text{ks}$ ). Sources with no spectroscopic redshift assigned are shown by their  $z_{phot}$  (orange and red squares). Above each panel, we show the distribution of  $m_{4.5}$  for the robust THRILS spectroscopic redshifts (blue with black border), the lower confidence THRILS redshifts (light blue with black hatching), and the photometric-only redshifts (i.e., non-detections, orange and red).

In each panel, we highlight the non-detection threshold in gray-shaded regions at both the full survey depth (left) and half the program depth (right). The shaded area is drawn at the magnitude of the faintest robustly-detected source,  $m_{4.5} = 29.3$  mag, for the full survey depth. For the half-depth, we find a detection threshold of  $m_{4.5} \simeq 28.25$  mag, nearly 1 dex shallower than the  $> 8$  hr full-integration time. We note that the two secure THRILS detections within the shaded region in the half-depth panel are unique, in that they are two EELGs whose very strong nebular lines are the reason they could be detected at such faint NIR magnitudes.

## 5. SURVEY SCIENCE GOALS

In the following sections, we outline the three key science cases that drove this observing program. As part of a broader discussion about the need for still-deeper NIR spectroscopy, we include example spectroscopy from each science case to showcase the improvements in sensitivity of the THRILS program ( $>8$  hr) compared to other programs in the EGS field that have had  $<1$  hr of

integration in this same filter and resolution (G395M),<sup>2</sup> such as CEERS (Arrabal Haro et al. in prep) and RUBIES (A. de Graaff et al. 2025).

### 5.1. Science Case 1: Probing the Nature of the IMF at Cosmic Dawn

Among the many predictions for the earliest galaxies is the notion that they should contain extremely low-metallicity (perhaps even primordial) stellar populations (e.g., J. Jaacks et al. 2018; B. Liu & V. Bromm 2020; A. Venditti et al. 2023). Such systems are expected to have a very different stellar IMF than the present-day Universe (e.g., V. Bromm 2013; R. S. Klessen & S. C. O. Glover 2023), with a “top-heavy” IMF (higher abundance of more massive stars) predicted to become dominant at these early times due to a combination of low metallicities and a rising CMB temperature floor (e.g., R. B. Larson 1998; V. Bromm et al. 2001a; C. J. Clarke & V. Bromm 2003; R. Schneider & K. Omukai 2010; S. Chon et al. 2021; P. Sharda & M. R. Krumholz 2022). While it is unclear whether we should expect to see truly metal-free stars with *JWST*, these observations now probe  $<300$  Myr after the Big Bang (e.g., R. P. Naidu et al. 2025a). It would be surprising if *JWST* observations did not reveal that the IMF began to evolve early. Top-heavy stellar populations have a ratio of UV luminosity to unit stellar mass that rises with the dominant stellar temperature. This lack of evolution is precisely what one would predict if a top-heavy IMF dominated the light from such early galaxies. In fact, S. L. Finkelstein et al. (2022b) found that the observed galaxy population was consistent with the expected evolution if the  $z > 10$  galaxies had their UV luminosities boosted by factors of  $\sim 2\times$  (see also L. Y. A. Yung et al. 2024), consistent with expectations from extremely metal-poor systems (XMP;  $Z < 3\%$   $Z_{\odot}$ ; e.g., A. Raiter et al. 2010; D. A. Berg et al. 2021). The advanced spectroscopic capabilities of *JWST* make these scenarios immediately testable, as stellar populations dominated by XMP (or zero-metallicity) stars would exhibit extremely high-ionization emission lines (e.g., A. H. Pawlik et al. 2011; K. Nakajima & R. Maiolino 2022).

For the first science case, THRILS obtained deep NIRSspec/MSA spectroscopy of a sample of *JWST*-discovered galaxies to probe their stellar populations. The observing constraints and targets (described in

<sup>2</sup> We note that these programs were intended to cover wide areas of their target fields, therefore their observing strategies were to use shallower integrations to accommodate a larger coverage on the sky. The comparison of these programs to THRILS is not to devalue these previous programs, but rather to emphasize the importance of deeper follow-up observations.

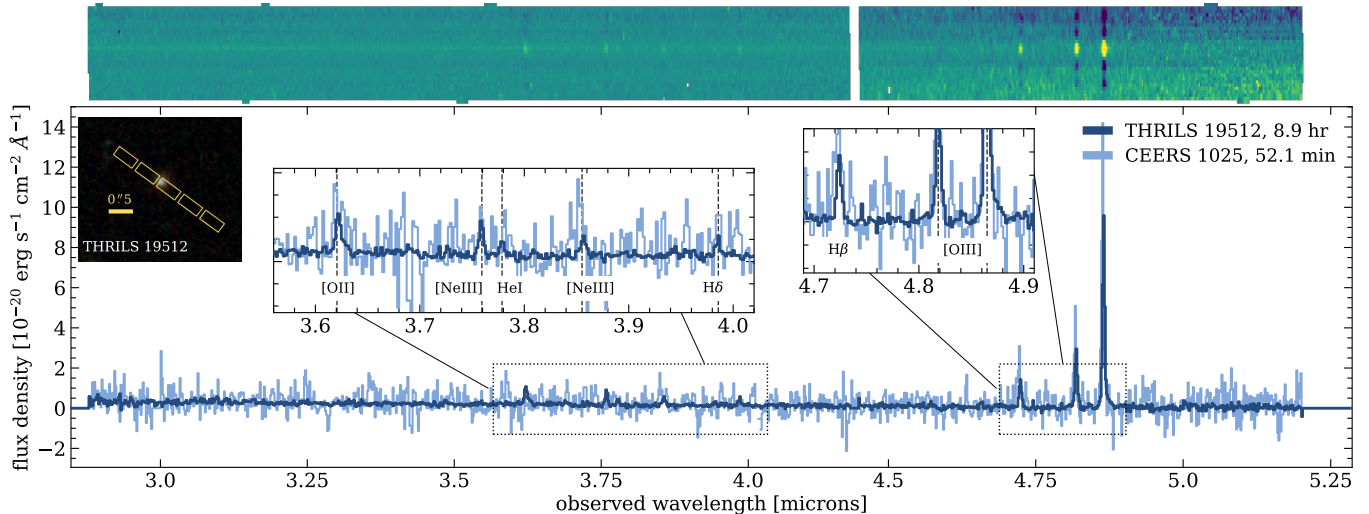


**Figure 4. Spectrum of a source from THRILs Science Case 1.** THRILs-19512 is a  $z = 8.7146$  galaxy initially observed with NIRSpec by the CEERS program (CEERS MPTID 1025; S. L. Finkelstein et al. 2024). The 2D spectrum from THRILs is shown across the top, and the 7-filter color image from CEERS is shown in the inset to the left with the THRILs NIRSpec shutter overlaid. The publicly available 1D CEERS spectrum (light blue, Arrabal Haro et al. in prep) has an exposure time of 52.1 min, while the THRILs optimally extracted 1D spectrum (dark blue) has an exposure time of 8.85 hours. Inset plots highlight the detections of He I  $\lambda 3890$  and H  $\delta$   $\lambda 4103$ , which were not possible in the shallower data.

§2.2) are optimized for both fainter sources and those that may host higher-ionization emission features. The latter intended to determine if signatures of ultra-low metallicities or intermediate-mass (growing) black holes were present (for which low-redshift analogs from N. J. Cleri et al. 2023b; G. M. Olivier et al. 2022; D. A. Berg et al. 2019 are valuable comparisons). Very high ionization emission requires a strong ionizing continuum – even in stellar populations dominated by extremely low metallicities coupled with a more “typical” IMF (e.g. P. Kroupa et al. 2013; G. Chabrier 2003), these spectral features would likely be weakly detected at best (see modeling comparisons in N. J. Cleri et al. 2025). Only in more extreme stellar population scenarios, i.e., XMPs prescribed by a top-heavy IMF (such as those from Ygdrasil, E. Zackrisson et al. 2011), would we expect a significantly strong detection of such high-ionization emission features.

A detailed study directly addressing the primary science in Science Goal 1 will be summarized in Hutchison et al. (in prep). As a visualization of other science enabled for these high- $z$  galaxies, here we showcase the improvements in sensitivity of the THRILs program ( $>8$  hr) compared to other programs in the EGS field that have had  $<1$  hr of integration time, such as CEERS (Arrabal Haro et al. in prep) and RUBIES (A. de Graaff et al. 2025). Figure 4 shows spectra for THRILs-19512, a high-redshift galaxy at  $z = 8.7146$  which CEERS first observed in the same grating/filter pair (G395M/F290LP; MPTID 1025). As a shallower

spectroscopic program, CEERS had only  $\sim 50$  minutes of integration time (light blue, Arrabal Haro et al. in prep), compared to the THRILs (dark blue) 8.85 hr on this same source. In the deeper THRILs spectrum, fainter lines such as He I  $\lambda 3890$  and H  $\delta$  are clearly detected, whereas in the shallower CEERS data, they fell below the noise threshold. We note that in this figure, we use publicly available CEERS data, which was reduced using different processes and pipeline versions, as well as variations in slitloss corrections, likely accounting for any apparent differences in the detected line flux measurements. The increase in depth and sensitivity enabled by THRILs yields a significant boost in science from these data. Additionally, and by design, more than half of the sources targeted as part of Science Case 1 in THRILs are fainter than  $m_H$  (F150W) = 27.5 mag. Detailed studies of faint early galaxies require the detection of the full suite of emission-line features, which is only possible with the sensitivity provided by observational depths similar to THRILs. See Hutchison et al. (in prep) and Davis et al. (in prep) for more details on the results from Science Case 1.

### 5.2. Science Case 2: Determining the Nature of Puzzling Broad-Line AGN Discovered with JWST

From ultra-dense gas to super-Eddington accretion, the origin, nature, and fate of newly-discovered Type 1 AGN candidates with JWST remain one of the most contested areas of inquiry in early black hole-galaxy co-evolution (K. Inayoshi 2025; E. Lambrides et al. 2024; I.

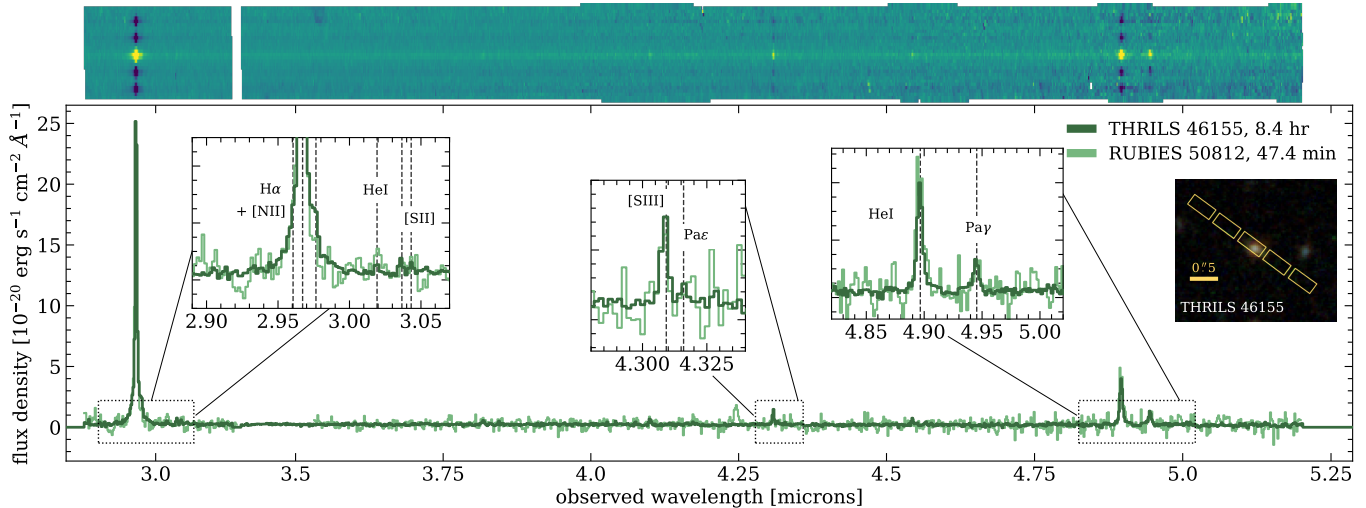


**Figure 5. Spectrum of an AGN from THRILs Science Case 2.** THRILs-46155 is a BLAGN at  $z = 3.5179$  that was first observed for 47.7 min by the RUBIES program (ID 50812; A. de Graaff et al. 2025). The 2D spectrum from THRILs (8.4 hr) is shown across the top, and the 7-filter color image from CEERS is shown in the inset to the right with the THRILs NIRSpec shutter overlaid. The publicly-available RUBIES data (light green) detects the broad component of  $H\alpha$   $\lambda 6564$  (A. J. Taylor et al. 2025a), but the deeper THRILs data (dark green) is needed to measure the fainter [S II]  $\lambda\lambda 6718, 6733$  and [S III]  $\lambda\lambda 9069, 9531$  doublet lines shown in the insets.

Juodžbalis et al. 2024; R. P. Naidu et al. 2025b; A. Lupi et al. 2024). The critical yet incomplete task of contextualizing high- $z$  BLAGN, including LRDs, within the broader landscape of high-redshift galaxies has made it difficult to determine the intersection between extreme ISM properties and extreme accretion properties. For LRDs specifically, the common characteristics that all interpretations aim to account for are a) peculiar “v-shaped” SEDs characterized by a puzzling UV excess alongside red *JWST*/NIRCam colors ( $m_{277} - m_{444} > 1.5$  mag, and an apparent Balmer break); b) broadened hydrogen Balmer emission ( $> 1000$  km s $^{-1}$ ); c) a general lack of multi-wavelength counterparts in the X-ray, sub-mm, and radio wavelengths; and d) a flat SED in the rest-frame NIR as inferred by *JWST*/MIRI (e.g., H. B. Akins et al. 2025; B. Wang et al. 2025a; P. G. Pérez-González et al. 2024b). A subset of LRDs are found to have deep Balmer absorption within the Balmer emission features (e.g., A. J. Taylor et al. 2025b) and, for the handful of these sources observed to sufficient depths, rich iron emission (e.g. R. E. Hviding et al. 2025; E. Lambrides et al. 2025). Part of the difficulty in concretely connecting the physical mechanisms that drive the rest-UV/optical spectral properties of both the new Type 1 BLAGN and LRD populations is the lack of spectral resolution and depth to sufficiently detail line emission on scales both close and far from the central emitting region.

With THRILs, we are characterizing the density, temperature, and line widths of several BLAGN candidates

(see Section 2.2). In addition to robustly measuring the kinematics of the broad-line region, we are also hunting for faint but important ISM-constraining lines (i.e., [N II]  $\lambda\lambda 6550, 6585$ , [S II]  $\lambda\lambda 6718, 6733$ , [O III]  $\lambda 4364$ ) to compare and contrast the ionization state of the BLAGN populations discovered with *JWST*. Here we highlight one of our AGN sources in Figure 5, THRILs-46155, which is a BLAGN source first observed by RUBIES with the ID 50812 (A. J. Taylor et al. 2025a; A. de Graaff et al. 2025). The THRILs  $> 8$  hr depth (dark green) enables the measurement of the [S II] and [S III] emission lines in this source, providing valuable metallicity-insensitive constraints on the ionization levels in this AGN (e.g., L. J. Kewley et al. 2019; R. L. Sanders et al. 2020). We note that in this figure, we use the publicly available RUBIES data, which was reduced using different processes and pipeline versions, as well as slitloss corrections, likely accounting for any apparent differences in the detected line flux measurements.

THRILs has already yielded significant surprises on this front, with the discovery of a rich series of faint iron features detected in a  $z \sim 7$  LRD (E. Lambrides et al. 2025) previously spectroscopically observed by shallower programs (M. Tang et al. 2025; B. Wang et al. 2025b). These lines uniquely constrain both the AGN nature of this source and provide new clues on the chemical enrichment history of LRD host galaxies. More details on the results from this Science Case will be presented in upcoming work by Davis et al. (in prep.) and Ganapathy et al. (in prep.).

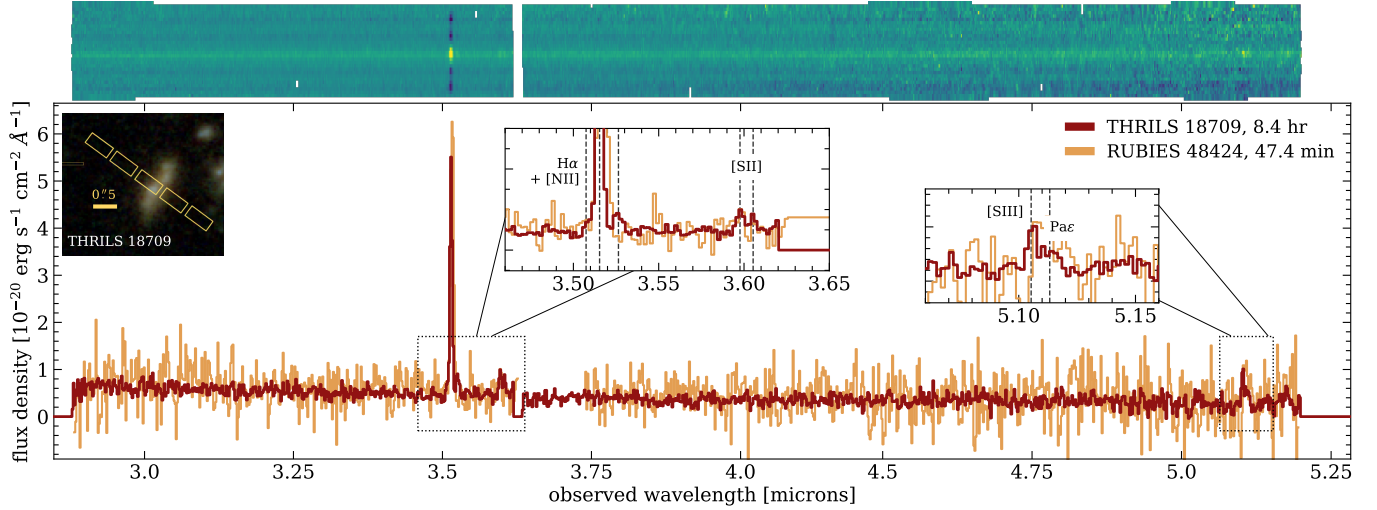


**Figure 6. Spectrum of a Massive Star-Forming Galaxy from THRILs Science Case 3.** THRILs-18709 is a massive galaxy at  $z = 4.355$  which was first observed for 47.7 min by the RUBIES program (ID 48424; A. de Graaff et al. 2025). The 2D spectrum from THRILs (8.4 hr) is shown across the top, and the 7-filter color image from CEERS is shown in the inset to the left with the THRILs NIRSpec shutter overlaid. The deeper THRILs spectrum (dark red) enables the disentangling of the [N II]  $\lambda\lambda 6550, 6585$  from the  $H\alpha$   $\lambda 6564$  line as shown in the inset. The THRILs spectrum also successfully measures the [S II]  $\lambda\lambda 6718, 6733$  doublet, which is within the noise of the publicly available RUBIES (light red) spectrum.

### 5.3. Science Case 3: SFHs of massive galaxies at $z > 4$

The emergence of massive galaxies in the early Universe has revealed that galaxies assembled stellar mass at earlier epochs than expected, with candidates selected from photometry with stellar mass  $\log(M/M_{\odot}) > 10$  forming as early as  $z \sim 9$  (e.g., I. Labbé et al. 2022). This population of candidate high-redshift massive galaxies is in non-negligible tension with current galaxy formation theories, as simulations have difficulty rapidly building up stellar masses to  $\log(M/M_{\odot}) > 10$  in  $< 1$  Gyr (e.g., C. L. Steinhardt et al. 2016; J. R. Weaver et al. 2022; C. C. Lovell et al. 2023; A. Ferrara et al. 2023). Photometry alone is insufficient to confirm the redshifts of these sources and recover their mass assembly histories with robustness. Age–dust–metallicity degeneracies make photometric SFH inferences largely prior-dominated (especially without a spectroscopic redshift; see discussion in e.g., P. G. Pérez-González et al. 2025), and often different star formation history (SFH) models with varying degrees of flexibility can fit broadband photometric points equally well (J. Leja et al. 2019; A. C. Carnall et al. 2019; K. Chworowsky et al. 2023, and references therein).

NIRSpec enables spectroscopic confirmation and SFH constraints via emission-line and Balmer-absorption measurements, which are critical for detecting quiescence in galaxies and characterizing the oldest stellar populations in high-redshift galaxies. The limited cosmic time available for the formation of these high-redshift galaxies means that their SFHs can be reliably

recovered using complex, flexible, yet physically motivated non-parametric models. The flexibility of non-parametric models allows for the capture of rapid burst and quenching episodes seen at high redshifts (T. J. Looser et al. 2023; R. Endsley et al. 2025; A. Covelopaz et al. 2025; studies based upon NIRCcam photometry and/or NIRSpec prism spectra), while simultaneously avoiding biases of an assumed fixed SFH shape. Related to the latter point, there are established best practices in literature for avoiding biases and systematic uncertainties in inferred parameters from stellar population synthesis modeling, as well as mitigating the age-metallicity-dust degeneracy in spectroscopic modeling. Such best practices include ensuring that multiple emission lines across a long wavelength arm are used for dust corrections, rest-frame UV to optical signatures are utilized to measure the age of stellar populations, etc. Many key spectral features can place limits on the star-formation/mass assembly and quenching timescales (e.g., instantaneous dust-unobscured star-formation rates and the ages of a diversity of stellar populations). Recent bursts of star formation are well traced by  $H\alpha$  (and to some extent  $H\beta + [O III]$ ), placing limits on star formation within the most recent 5–20 Myr. For galaxy populations that have ceased forming stars, the  $H\delta$  absorption line (and other strong Balmer absorption lines) can indicate a post-starburst phase ( $\sim 100 - 500$  Myr after the initial burst) and the  $3650\text{\AA}$  Balmer break (or  $D_n(4000)$ ) places limits on older stellar populations of  $\sim 300 - 500$  Myr before observation

(e.g., M. L. Balogh et al. 1999; B. M. Poggianti et al. 1999, 2009; D. Vergani et al. 2010; A. S. Mansheim et al. 2017).

THRILS is designed to constrain the mass assembly histories of these extreme objects and to further our understanding of their formation pathways by distinguishing among strong emission-line features, the Balmer break, and absorption features. Critically, the deblending of emission lines in proximity to each other –  $H\alpha$  + [N II] and  $H\beta$  + [O III] – is achieved in THRILS, and offers precise measurements of SFRs and physical conditions of the nebular regions within these systems (e.g., see A. E. Shapley et al. 2025 for state-of-the-art nebular line diagnostics in high- $z$  galaxies calibrated to *JWST* observations). While studies like A. Covelo-Paz et al. (2025) acknowledge recent star formation in starburst/post-starburst galaxies with blended  $H\alpha$  + [N II] measurements, THRILS is designed to definitively constrain SF at timescales of 10–20 Myr, and disentangle it from SF timescales of 100–200 Myr (via extant rest-frame UV measurements).

Here we show one of our massive galaxies from Science Case 3, THRILS-18709, first observed by RUBIES with ID 48424 (A. de Graaff et al. 2025). The THRILS spectrum (dark red) achieves the depth required to detect and disentangle the [N II] emission from the  $H\alpha$  line profile, enabling a measurement of the metallicity in this source. Figure 6 also shows the successful detection of the [S II] doublet and separation of [S III]  $\lambda$ 9531 from Pa $\epsilon$  – providing limits on the ionization levels in this source and further limiting the effect of degeneracies in the mass-weighted ages of stars and in gas phase metallicity.

By combining spectroscopy with flexible, non-parametric SFH inference, THRILS will measure key formation timescales and burst durations, thereby confirming the presence of a diversity of stellar populations in massive galaxies in the early Universe, and simultaneously constraining how rapidly they assembled. These results will also directly inform whether star formation at high redshifts proceeds in a different regime than in lower-redshift galaxies. See Chworowsky et al. (in prep) for more results from Science Case 3.

## 6. CONCLUSION

In this paper, we summarize the THRILS survey goals, program execution, data reduction, redshift measurements, and detection threshold. We provide a redshift catalog for 89 THRILS sources with robust redshift measurements, visually vetted by the team. We also present the additional 81 sources that show no detectable signal in our data, despite the depth of our observations. The

THRILS observational constraints yield NIRSpec detection thresholds of  $m_{4.5\mu m} = 29.3$  for an 8 hr integration and  $m_{4.5\mu m} \simeq 28.25$  for  $\sim 4$  hr, which can directly inform future deep spectroscopy surveys. We also highlight faint emission-line detections that are only possible with the deeper spectroscopy, underscoring the need for greater depth in future programs to answer key science questions across a wide range of science goals in the high- $z$  Universe.

## ACKNOWLEDGMENTS

We acknowledge that a significant part of our work is done on stolen land, and we support the efforts of Land Back and true stewardship to those same peoples whose land is occupied. The PIs also note that we do not use the full name of *JWST* due to the person after whom this telescope is named and their role as NASA administrator during the “Lavender Scare”, as per the *#RenameJWST* protest movement.

The THRILS team would like to thank our program coordinators (PCs), Carol Rodriguez and Blair Porterfield, for their help with planning and executing our program. We would also like to thank Dan Coe, our Contact Scientist (CS), for his valuable insight and assistance with designing our MPT.

We thank the programs that came before us, which enabled the cataloging of hundreds of thousands of galaxies in this field, using both ground- and space-based telescopes, both imaging and spectroscopy. Such programs include CANDELS, MOSDEF, UVCANDELS, CEERS, RUBIES, and MEGA. We also thank efforts to create resources for the community, such as the Dawn *JWST* Archive (DJA), which was used in this work to check previous *JWST* redshifts for our catalog.

TAH’s research is supported by an appointment to the NASA Postdoctoral Program at the NASA Goddard Space, administered by Oak Ridge Associated Universities under contract with NASA. RLL appreciates support from a Giacconi Fellowship at the Space Telescope Science Institute, which is operated by the Association of Universities for Research in Astronomy, Inc., under NASA contracts NAS 5-26555 and NAS5-03127.

*Facilities:* *JWST* (NIRCam, NIRSpec, & MIRI), HST (ACS, WFC3), Spitzer (Ch1, Ch2), Keck (MOSFIRE, DEIMOS)

*Software:* astropy (Astropy Collaboration et al. 2013, 2018, 2022), Cloudy (G. J. Ferland et al. 2013), Source Extractor (E. Bertin & S. Arnouts 1996) TOPCAT (M. Taylor 2011), Dense Basis (K. G. Iyer et al. 2021), IDL (W. B. Landsman 1993), *JWST* Pipeline (H.

Bushouse et al. 2022), SAOImage DS9 ( Smithsonian Astrophysical Observatory 2000)

## APPENDIX

Here we provide a spectroscopic redshift catalog for all 89 sources robustly detected in the THRILS survey (Table 3). This table also includes 13 additional sources with either continuum or emission-line detections but lacking a redshift measurement, as described in §4.1. Included columns are the MPT ID from THRILS, RA and Dec coordinates of the source, a measured spectroscopic redshift ( $z_{spec}$ ) from the THRILS data, a  $z_{spec}$  quality grade, the total integration time on source, the target category (Primary, Filler, or Contaminant), photometry in 3 bandpasses ( $m_H$ ,  $m_{3.6}$ , and  $m_{4.5}$ ), and any prior photometric ( $z_{phot}$ ) and spectroscopic ( $z_{spec}$ ) redshift information available (as described in §2.1). Sources that have *HST*-only derived  $z_{phot}$  measurements, as they lie outside the CEERS NIRCam coverage (S. L. Finkelstein et al. 2025), are marked with an asterisk (\*). Table footnotes denote the reference catalogs or publications from which the previous  $z_{phot}$  and  $z_{spec}$  measurements are taken.

Separately, we provide a table of the 81 non-detections in THRILS (Table 4) as described in §4.2. The format of this table is the same as Table 3; however we omit the redshift measurement and grade.

Machine-readable tables of both the spectroscopic redshift and non-detection catalogs are provided with the publication of this paper.

Table 3. The THRILS Survey Redshift Catalog

THRILS ID <sub>MPT</sub>	Coordinates			THRILS			Magnitudes			Prior Redshifts	
	RA	DEC	$z_{spec}$	Grade	ExpTime [s]	Category	H	3.60	4.50	$z_{phot}$	$z_{spec}$
102659	214.943146	52.94244	11.41	2	31862	Primary	28.4±0.1	27.95±0.04	27.68±0.04	11.6 <sup>10.0</sup> <sub>10.0</sub>	11.42 <sup>a</sup>
117286	214.977181	52.926547	9.0307	1	15931	Filler	28.6±0.1	28.78±0.09	29.0±0.2	9.0 <sup>9.9</sup> <sub>1.4</sub>	-1
92641	214.823994	52.884186	8.93	1	15056	Filler	28.78±0.06	28.86±0.04	28.9±0.05	8.0 <sup>8.6</sup> <sub>1.8</sub>	-1
97442	214.838696	52.882226	8.929	3	30111	Primary	29.2±0.1	28.96±0.06	28.28±0.03	9.0 <sup>10.0</sup> <sub>8.7</sub>	-1
37717	214.93864	52.911749	8.7578	3	31862	Primary	26.48±0.02	26.76±0.01	26.24±0.009	9.0 <sup>9.0</sup> <sub>8.8</sub>	8.768 <sup>b</sup>
19512	214.967531	52.932951	8.7146	3	31862	Primary	26.1±0.02	26.46±0.01	26.1±0.008	9.0 <sup>8.8</sup> <sub>8.6</sub>	8.717 <sup>b</sup>
81287	214.995191	52.903856	8.6679	3	31862	Primary	28.19±0.09	28.58±0.07	27.84±0.05	10.5 <sup>10.0</sup> <sub>9.0</sub>	-1
115593	214.855926	52.846312	8.658	2	15056	Filler	29.4±0.1	29.7±0.09	29.08±0.06	8.0 <sup>9.3</sup> <sub>8.1</sub>	-1
107103	214.944763	52.931451	7.9229	3	31862	Primary	27.94±0.04	28.63±0.04	27.93±0.02	8.0 <sup>8.2</sup> <sub>7.9</sub>	7.921 <sup>b</sup>
146988	214.992762	52.930886	7.9	3	15931	Filler	26.5±0.1	-1	-1	6.0 <sup>7.6*</sup> <sub>1.4</sub>	-1
111728	214.911092	52.897315	7.4788	3	31862	Primary	27.97±0.04	28.25±0.03	27.4±0.02	7.0 <sup>7.4</sup> <sub>7.3</sub>	-1
117694	214.914025	52.88102	7.146	3	15056	Primary	28.75±0.09	28.5±0.04	27.81±0.03	7.0 <sup>7.4</sup> <sub>7.2</sub>	-1
44534	214.837993	52.863454	6.967	3	15056	Primary	27.49±0.05	26.73±0.02	26.62±0.01	7.0 <sup>7.4</sup> <sub>6.9</sub>	-1
96512	214.835418	52.882867	6.87	3	30111	Filler	28.36±0.09	28.81±0.09	29.2±0.1	7.0 <sup>7.4</sup> <sub>6.8</sub>	-1
44905	214.951073	52.93891	6.778	3	15931	Filler	28.69±0.06	28.14±0.02	28.74±0.05	7.0 <sup>6.7</sup> <sub>6.7</sub>	-1
46036	214.906056	52.893278	6.75	3	30111	Primary	27.9±0.1	26.89±0.02	27.57±0.03	7.0 <sup>6.7</sup> <sub>6.7</sub>	-1
47007	214.942703	52.905126	6.737	3	31862	Primary	28.6±0.1	27.2±0.02	28.13±0.04	7.0 <sup>6.7</sup> <sub>6.7</sub>	-1
16050	214.946731	52.900509	6.734	3	31862	Primary	26.1±0.02	25.48±0.009	25.79±0.01	7.0 <sup>6.9</sup> <sub>6.8</sub>	-1
11751	214.910857	52.852141	6.73	3	30111	Primary	24.39±0.01	25.87±0.03	26.28±0.06	6.0 <sup>6.3</sup> <sub>6.2</sub>	-1
114396	214.892867	52.86516	6.686	3	30111	Primary	29.0±0.07	28.47±0.03	29.32±0.06	7.0 <sup>6.7</sup> <sub>6.6</sub>	6.7072 <sup>b</sup>
46403	214.892249	52.877403	6.68	3	30111	Primary	26.69±0.02	24.38±0.002	23.98±0.001	7.0 <sup>7.1</sup> <sub>6.8</sub>	6.6832 <sup>c</sup>
43224	214.920965	52.940749	6.673	3	15931	Filler	27.41±0.04	26.59±0.01	26.99±0.01	7.0 <sup>6.7</sup> <sub>1.4</sub>	-1
44635	214.951621	52.943014	6.65	3	15931	Filler	27.36±0.05	26.83±0.02	27.38±0.04	7.0 <sup>6.7</sup> <sub>6.6</sub>	-1
25501	214.863029	52.889436	6.572	3	15056	Primary	26.19±0.02	25.29±0.008	25.92±0.009	7.0 <sup>6.6</sup> <sub>6.6</sub>	6.579 <sup>c</sup>
44762	214.888951	52.896706	6.534	3	30111	Primary	27.32±0.04	26.81±0.01	27.23±0.02	7.0 <sup>6.6</sup> <sub>6.5</sub>	-1
48544	214.912338	52.858846	6.53	3	30111	Primary	28.34±0.07	27.44±0.02	28.28±0.05	7.0 <sup>6.7</sup> <sub>6.6</sub>	-1
23361	214.880968	52.891218	6.483	3	30111	Primary	26.33±0.02	25.52±0.007	26.16±0.01	7.0 <sup>6.6</sup> <sub>6.6</sub>	6.4858 <sup>c</sup>

Table 3 continued

Table 3 (continued)

THRILS ID <sub>MPT</sub>	Coordinates			THRILS			Magnitudes			Prior Redshifts	
	RA	DEC	$z_{spec}$	Grade	ExpTime [s]	Category	H	3.60	4.50	$z_{phot}$	$z_{spec}$
82535	214.996363	52.907148	6.459	2	15931	Filler	23.14±0.02	25.23±0.07	25.14±0.07	6.0 <sup>6.3</sup> <sub>6.2</sub>	-1
119163	214.949399	52.901025	6.21	2	15931	Filler	29.6±0.7	27.6±0.06	29.4±0.4	6.8 <sup>10.0</sup> <sub>4.7</sub>	-1
34328	214.991306	52.890046	6.183	3	31862	Primary	27.3±0.03	26.28±0.008	27.01±0.02	6.0 <sup>6.4</sup> <sub>6.2</sub>	6.1872 <sup>c</sup>
140096	214.967647	52.938116	6.1385	2	15931	Filler	26.82±0.07	-1	25.8±0.5	6.0 <sup>7.0</sup> <sub>8.1</sub> *	-1
82330	214.910771	52.847172	6.011	3	15056	Filler	29.3±0.2	28.21±0.05	28.07±0.05	6.0 <sup>6.0</sup> <sub>3.9</sub>	-1
97420	214.855414	52.894118	5.993	3	30111	Filler	28.5±0.2	27.82±0.08	29.0±0.2	7.0 <sup>6.7</sup> <sub>6.2</sub>	-1
22417	214.89087	52.893244	5.98	3	30111	Primary	26.25±0.02	25.71±0.008	25.82±0.008	6.0 <sup>6.4</sup> <sub>6.2</sub>	5.986 <sup>c</sup>
48907	214.975838	52.897791	5.94	3	15931	Filler	26.47±0.03	25.64±0.01	26.25±0.02	6.0 <sup>6.4</sup> <sub>6.1</sub>	-1
49055	214.903689	52.844912	5.805	3	30111	Primary	27.8±0.05	27.0±0.02	27.45±0.03	6.0 <sup>6.5</sup> <sub>6.2</sub>	5.805 <sup>b</sup>
44025	214.823382	52.860373	5.751	3	30111	Primary	26.85±0.04	26.58±0.02	26.85±0.03	6.0 <sup>6.2</sup> <sub>6.0</sub>	5.7558 <sup>c</sup>
49043	214.995872	52.910405	5.683	3	31862	Primary	27.41±0.03	26.79±0.01	27.06±0.02	6.0 <sup>5.9</sup> <sub>5.6</sub>	-1
78835	214.986859	52.891884	5.675	3	15931	Filler	29.4±0.3	27.64±0.03	27.89±0.05	6.0 <sup>6.3</sup> <sub>4.5</sub>	-1
87309	214.976767	52.90824	5.641	3	15931	Filler	29.0±-1.0	27.32±0.03	27.77±0.07	7.0 <sup>6.8</sup> <sub>6.3</sub>	-1
38124	214.95186	52.928259	5.482	3	31862	Primary	26.44±0.03	26.01±0.01	26.31±0.009	6.0 <sup>5.9</sup> <sub>5.3</sub>	5.4805 <sup>c</sup>
101567	214.831734	52.867166	5.322	3	30111	Primary	28.59±0.09	28.54±0.06	27.85±0.03	7.0 <sup>7.4</sup> <sub>7.0</sub>	-1
29871	214.831188	52.886545	5.32	3	30111	Primary	25.72±0.02	24.95±0.007	24.89±0.006	5.0 <sup>5.5</sup> <sub>5.4</sub>	-1
45758	214.860947	52.864547	5.272	3	30111	Primary	28.1±0.1	27.19±0.03	27.22±0.04	5.0 <sup>5.3</sup> <sub>1.5</sub>	-1
40467	214.923949	52.948385	5.2715	3	31862	Primary	26.75±0.03	25.76±0.007	25.56±0.005	5.0 <sup>5.4</sup> <sub>5.2</sub>	5.271 <sup>c</sup>
49400	215.000179	52.907742	5.12	3	31862	Primary	27.16±0.03	26.57±0.009	25.48±0.005	5.0 <sup>5.2</sup> <sub>5.1</sub>	-1
44774	214.828433	52.853442	5.101	3	30111	Primary	27.78±0.04	26.74±0.01	25.97±0.007	5.0 <sup>5.2</sup> <sub>5.1</sub>	-1
43139	214.926194	52.945551	5.087	3	31862	Primary	26.82±0.03	25.76±0.009	25.54±0.005	5.0 <sup>5.3</sup> <sub>5.1</sub>	-1
34913	214.981422	52.893632	5.077	3	15931	Filler	26.73±0.02	26.82±0.01	26.45±0.01	5.0 <sup>5.2</sup> <sub>5.1</sub>	-1
21489	214.926772	52.914039	5.071	3	31862	Primary	26.87±0.02	26.74±0.01	26.17±0.005	5.0 <sup>5.2</sup> <sub>5.1</sub>	-1
107963	214.839139	52.854132	4.99	3	30111	Primary	28.13±0.09	28.13±0.05	28.22±0.07	5.0 <sup>5.1</sup> <sub>4.9</sub>	-1
30374	214.915251	52.944979	4.894	3	31862	Primary	24.54±0.01	24.08±0.005	24.21±0.005	1.0 <sup>1.0</sup> <sub>0.91</sub>	-1
42648	214.913796	52.942971	4.89	3	31862	Primary	24.55±0.01	23.08±0.002	22.94±0.002	6.0 <sup>5.6</sup> <sub>5.4</sub>	-1
97936	214.917989	52.937245	4.889	3	31862	Filler	29.5±0.3	27.65±0.03	27.78±0.03	5.0 <sup>6.5</sup> <sub>6.3</sub>	4.888 <sup>b</sup>
44527	214.942535	52.937728	4.887	3	10621	Contaminant	26.62±0.04	26.39±0.02	26.61±0.02	5.0 <sup>4.8</sup> <sub>4.7</sub>	-1
41237	214.917184	52.949369	4.88	3	31862	Primary	26.89±0.03	26.08±0.01	26.09±0.01	5.0 <sup>4.9</sup> <sub>4.7</sub>	-1

Table 3 continued

Table 3 (continued)

THRILs	Coordinates			THRILs			Magnitudes			Prior Redshifts		
	ID <sub>MPT</sub>	RA	DEC	z <sub>spec</sub>	Grade	ExpTime [s]	Category	H	3.60	4.50	z <sub>phot</sub>	z <sub>spec</sub>
105834	214.8421	52.862287		4.81	1	30111	Filler	-1	30.2±0.1	29.7±0.1	9.6 <sup>20.0</sup> <sub>7.7</sub>	-1
105963	214.889044	52.895062		4.809	3	15056	Primary	28.6±0.1	28.39±0.06	29.2±0.1	5.0 <sup>4.8</sup> <sub>4.3</sub>	-1
37813	214.898922	52.885389		4.808	3	30111	Primary	27.33±0.04	26.69±0.01	26.95±0.01	5.0 <sup>4.7</sup> <sub>4.5</sub>	4.8082 <sup>c</sup>
100485	214.82091	52.861374		4.76	3	30111	Primary	28.6±0.2	27.33±0.04	27.62±0.05	5.0 <sup>4.8</sup> <sub>4.3</sub>	-1
17121	214.949419	52.907867		4.555	3	31862	Primary	25.1±0.01	24.14±0.003	24.22±0.004	5.0 <sup>4.8</sup> <sub>4.7</sub>	4.561 <sup>b</sup>
43853	214.919841	52.931443		4.524	3	15931	Filler	27.1±0.07	26.77±0.01	27.58±0.02	5.0 <sup>4.8</sup> <sub>4.6</sub>	-1
47014	214.888082	52.866244		4.484	3	15056	Filler	28.08±0.05	27.39±0.02	27.53±0.02	4.0 <sup>4.6</sup> <sub>4.1</sub>	-1
22246	214.943956	52.929792		4.478	3	31862	Primary	25.12±0.02	23.61±0.003	23.77±0.003	4.0 <sup>4.6</sup> <sub>4.3</sub>	-1
43708	214.938903	52.946747		4.397	3	15931	Filler	28.0±0.1	27.41±0.03	27.46±0.04	5.0 <sup>4.7</sup> <sub>4.2</sub>	-1
105849	214.835706	52.857677		4.3952	2	15056	Primary	28.66±0.08	28.12±0.03	28.78±0.06	5.0 <sup>4.8</sup> <sub>4.4</sub>	-1
24975	214.940291	52.941319		4.39	3	31862	Primary	25.36±0.009	24.7±0.003	25.16±0.004	5.0 <sup>4.9*</sup> <sub>4.5</sub>	-1
18709	214.858817	52.851472		4.355	3	30111	Primary	25.1±0.01	24.29±0.005	24.29±0.004	5.0 <sup>4.7</sup> <sub>4.5</sub>	4.3618 <sup>c</sup>
20464	214.858837	52.860404		4.352	3	30111	Filler	25.35±0.02	23.26±0.002	23.12±0.002	2.0 <sup>2.2</sup> <sub>2.5</sub>	4.3574 <sup>c</sup>
48965	214.973876	52.895808		4.114	3	31862	Primary	26.99±0.04	26.68±0.02	27.22±0.04	4.0 <sup>4.4</sup> <sub>4.2</sub>	-1
27259	214.918383	52.93789		3.912	3	31862	Primary	26.29±0.03	24.13±0.004	23.82±0.002	4.0 <sup>3.3</sup> <sub>3.8</sub>	-1
109756	214.887869	52.884643		3.7874	2	15056	Filler	30.7±0.4	30.19±0.08	31.4±0.3	5.0 <sup>6.7</sup> <sub>6.2</sub>	-1
24728	214.882084	52.898666		3.763	3	30111	Primary	24.9±0.01	23.86±0.003	23.71±0.002	4.0 <sup>3.2</sup> <sub>3.9</sub>	-1
118986	214.881081	52.852971		3.636	3	30111	Filler	28.28±0.09	28.14±0.05	28.26±0.06	4.0 <sup>4.4</sup> <sub>3.7</sub>	-1
13817	214.88459	52.844341		3.624	3	30111	Primary	24.84±0.007	24.46±0.005	24.27±0.003	4.0 <sup>4.2</sup> <sub>4.2</sub>	-1
46155	214.84549	52.848281		3.5179	3	30111	Primary	27.29±0.03	26.22±0.007	25.73±0.005	4.0 <sup>3.6</sup> <sub>3.5</sub>	3.5186 <sup>c</sup>
38893	214.9361	52.930684		3.3759	3	15931	Filler	27.11±0.03	27.72±0.03	27.3±0.02	3.0 <sup>3.4</sup> <sub>3.4</sub>	-1
23103	214.940797	52.93229		3.3042	3	15931	Filler	26.62±0.02	27.35±0.02	27.06±0.01	3.0 <sup>3.4</sup> <sub>3.4</sub>	-1
16295	214.896148	52.865738		3.2387	3	15056	Filler	25.18±0.006	24.65±0.002	24.51±0.002	3.0 <sup>3.3</sup> <sub>3.2</sub>	-1
18945	214.917581	52.894662		3.218	3	15931	Filler	26.68±0.02	26.56±0.01	26.48±0.01	3.0 <sup>3.2</sup> <sub>3.0</sub>	-1
42514	214.853252	52.901552		3.025	3	30111	Primary	24.8±0.009	23.67±0.003	23.48±0.002	4.0 <sup>4.3</sup> <sub>4.1</sub>	-1
13658	214.974102	52.905943		2.6136	3	31862	Primary	22.14±0.002	20.71±0.0008	20.21±0.0007	2.0 <sup>2.4</sup> <sub>2.3</sub>	2.6136 <sup>c</sup>
46649	214.857621	52.849534		1.918	2	10037	Contaminant	24.5±0.007	24.63±0.006	24.66±0.005	2.0 <sup>1.9</sup> <sub>1.7</sub>	-1
23870	214.950243	52.942729		1.279	1	10621	Contaminant	25.47±0.01	25.53±0.01	25.62±0.01	1.0 <sup>1.3</sup> <sub>1.2</sub>	-1
29328	214.834268	52.893785		0.7	2	30111	Primary	19.17±0.001	18.79±0.001	19.2±0.0007	0.7 <sup>0.73</sup> <sub>0.67</sub>	0.7328 <sup>d</sup>

Table 3 continued

Table 3 (continued)

THRILS ID <sub>MPT</sub>	Coordinates		THRILS			Magnitudes			Prior Redshifts		
	RA	DEC	$z_{spec}$	Grade	ExpTime [s]	Category	H	3.60	4.50	$z_{phot}$	$z_{spec}$
137586	215.003142	52.896297	0.0	1	5310	Contaminant	16.15±8e-06	16.93±0.0001	17.31±0.0002	0.01 <sup>0.02</sup> <sub>0.01</sub>	-1
156965	214.987478	52.89089	0.0	1	31862	Primary	19.06±0.0002	19.85±0.002	20.18±0.002	0.04 <sup>0.05*</sup> <sub>0.03</sub>	-1
21240	214.947976	52.925768	0.0	1	31862	Primary	20.64±0.004	21.46±0.002	21.76±0.0007	0.01 <sup>0.04</sup> <sub>0.01</sub>	-1
17639	214.91385	52.884142	0.0	1	30111	Primary	21.24±0.002	22.14±0.0009	22.41±0.0006	6.06 <sup>2</sup> <sub>1</sub>	-1
136596	215.00334	52.895862	-1.0	0	15931	Filler	22.05±0.003	-1	-1	5.0 <sup>4.6*</sup> <sub>4.5</sub>	-1
27920	214.854892	52.896851	-1.0	0	15056	Filler	25.48±0.009	25.27±0.006	25.39±0.006	4.0 <sup>4.2</sup> <sub>4.0</sub>	-1
46370	214.971028	52.933685	-2.0	0	15931	Filler	25.16±0.01	25.05±0.008	25.19±0.02	1.0 <sup>1.3</sup> <sub>1.1</sub>	-1
14536	214.977299	52.913015	-2.0	0	15931	Filler	27.02±0.05	27.04±0.03	27.1±0.05	0.0 <sup>2.7</sup> <sub>0.19</sub>	2.2107 <sup>e</sup>
141538	214.983922	52.944899	-2.0	0	15931	Filler	27.1±0.09	27.5±0.9	28.0±1.0	3.0 <sup>3.4*</sup> <sub>1.1</sub>	-1
38368	214.96954	52.944872	-2.0	0	15931	Filler	27.62±0.03	28.81±0.04	28.76±0.04	0.0 <sup>0.07</sup> <sub>0.01</sub>	-1
118431	214.918319	52.880803	-2.0	0	15056	Filler	28.0±0.1	28.12±0.09	28.2±0.1	5.0 <sup>3.5</sup> <sub>2</sub>	-1
116521	214.888015	52.866342	-2.0	0	10037	Filler	29.4±0.2	29.7±0.2	32.0±1.0	0.0 <sup>6.8</sup> <sub>0.43</sub>	-1
114003	214.887211	52.862043	-2.0	0	30111	Primary	28.7±0.1	28.6±0.07	28.22±0.04	11.4 <sup>10.0</sup> <sub>10.0</sub>	2.8884 <sup>c</sup>
9528	215.003141	52.896296	-3.0	0	5310	Contaminant	16.0±-1.0	17.0±-1.0	18.0±-1.0	0.5 <sup>0.48*</sup> <sub>0.45</sub>	-1
21981	214.9431	52.925335	-3.0	0	15931	Filler	21.83±0.003	21.45±0.002	21.68±0.001	1.0 <sup>1.2</sup> <sub>1.1</sub>	-1
20223	214.912872	52.897786	-3.0	0	15931	Filler	25.5±0.02	25.42±0.01	25.43±0.01	2.0 <sup>1.6</sup> <sub>1.4</sub>	-1
48447	214.916502	52.862885	-3.0	0	30111	Filler	26.7±0.05	26.1±0.02	25.95±0.02	3.0 <sup>3.0</sup> <sub>1.8</sub>	-1

NOTE—Full redshift catalog for the 89 sources with spectroscopic redshift measurements in the THRILS data, as well as the 13 additional sources with detectable lines ( $z_{spec} = -2$ ) or detected continuum ( $z_{spec} = -3$ ) but no discernible redshift. We note that for all  $z_{spec}$  from the THRILS program, the redshift uncertainty is 0.0003. Sources with a  $z_{spec} = 0$  are likely stars or brown dwarfs. Description of Columns: 1) ID in the THRILS MPT, 2-3) Coordinates, 4-5) Measured  $z_{spec}$  in THRILS and grade for this redshift as described in §4.1, 6-7) Exposure time and target category for the source as described in §2.2, 8-10) Magnitude of the source in 3 representative bands as described in §2.1, 11-12) Prior measurements of  $z_{phot}$  and  $z_{spec}$  from ancillary data as described in §2.1.

\* Sources with *HST* only derived  $z_{phot}$  measurements as they do not have *JWST*/NIRCam coverage.

<sup>a</sup> *JWST* DDT 2750 (P. Arrabal Haro et al. 2023a).

<sup>b</sup> CEERS (Arrabal Haro et al., in prep).

<sup>c</sup> DJA (A. de Graaff et al. 2024; K. E. Heintz et al. 2024).

<sup>d</sup> CANDELS (M. Stefanon et al. 2017).

<sup>e</sup> 3DHST (G. B. Brammer et al. 2012)

**Table 4.** Non-Detections from the THRILs Survey

THRILs	Coordinates		THRILs		Magnitudes			Prior Redshifts		
	ID <sub>MPT</sub>	RA	DEC	ExpTime [s]	Category	H	3.60	4.50	$z_{phot}$	$z_{spec}$
127239	214.85961	52.858029	15056	Filler	-1	-1	-1	-1	6.0611 <sup>a</sup>	
136697	215.003204	52.896604	15931	Filler	23.5±0.003	-1	-1	5.0 <sub>5.4</sub> <sup>5.8*</sup>	-1	
139799	214.948036	52.926073	10621	Contaminant	25.7±0.07	-1	-1	2.0 <sub>1.4</sub> <sup>8.0*</sup>	-1	
160204	214.841267	52.891728	15056	Filler	27.17±0.07	-1	-1	5.0 <sub>2.5</sub> <sup>5.4*</sup>	-1	
139366	214.9154	52.904181	15931	Filler	27.5±0.1	-1	-1	10.5 <sub>3.2</sub> <sup>10.0*</sup>	-1	
160727	214.913099	52.941113	15931	Filler	27.7±0.1	-1	-1	3.0 <sub>2.2</sub> <sup>10.0*</sup>	-1	
127087	214.949399	52.908	21241	Contaminant	29.0±-1.0	-1	-1	5.0 <sub>-1.0</sub> <sup>-1.0*</sup>	-1	
143034	214.921523	52.895192	31862	Filler	27.6±0.1	28.0±3.0	-1	10.6 <sub>10.0</sub> <sup>10.0*</sup>	-1	
113779	214.86049	52.855005	30111	Filler	30.4±0.6	29.3±0.2	-1	17.4 <sub>6.4</sub> <sup>20.0</sup>	-1	
105741	214.88741	52.894714	10037	Filler	30.3±0.3	29.8±0.1	-1	6.7 <sub>2.8</sub> <sup>20.0</sup>	-1	
115794	214.9694	52.926311	10621	Contaminant	31.0±1.0	30.2±0.2	-1	17.0 <sub>5.5</sub> <sup>20.0</sup>	-1	
104831	214.831237	52.857013	10037	Contaminant	30.5±0.4	30.6±0.3	-1	0.6 <sub>0.85</sub> <sup>10.0</sup>	-1	
110862	214.947994	52.925387	10621	Contaminant	28.76±0.06	31.0±0.2	-1	7.0 <sub>6.9</sub> <sup>8.0</sup>	-1	
18658	214.857584	52.849377	5019	Contaminant	22.38±0.002	22.38±0.002	22.37±0.001	1.0 <sub>1.1</sub> <sup>1.7</sup>	0.9137 <sup>b</sup>	
160549	214.840565	52.89058	15056	Filler	27.1±0.1	23.86±0.07	23.69±0.06	5.0 <sub>2.8</sub> <sup>4.8*</sup>	-1	
40281	214.848324	52.89162	15056	Filler	28.6±0.2	33.0±9.0	25.0±-1.0	5.0 <sub>5.1</sub> <sup>5.2</sup>	-1	
158240	214.83878	52.89779	15056	Filler	27.32±0.03	25.3±0.3	25.7±0.3	12.5 <sub>10.0</sub> <sup>10.0*</sup>	-1	
112097	214.913199	52.897737	15931	Filler	32.3±0.5	32.1±0.2	25.7±0.4	17.1 <sub>3.7</sub> <sup>20.0</sup>	-1	
10801	214.998121	52.909333	5310	Contaminant	26.49±0.02	26.32±0.01	26.28±0.01	2.0 <sub>2.0</sub> <sup>2.6</sup>	-1	
38054	214.933701	52.914233	15931	Filler	26.6±0.02	26.38±0.008	26.33±0.008	3.0 <sub>2.7</sub> <sup>3.0</sup>	-1	
45468	214.926827	52.914352	10621	Contaminant	26.24±0.03	26.2±0.01	26.46±0.01	0.7 <sub>0.55</sub> <sup>0.76</sup>	-1	
44514	214.942513	52.937886	15931	Filler	26.68±0.04	26.52±0.02	26.56±0.02	5.0 <sub>4.8</sub> <sup>5.8</sup>	-1	
41708	214.839797	52.901349	30111	Primary	27.4±0.1	26.66±0.04	26.75±0.05	5.0 <sub>1.3</sub> <sup>5.4</sup>	-1	
44772	214.93045	52.925902	15931	Filler	26.24±0.03	26.58±0.02	26.85±0.02	1.0 <sub>0.94</sub> <sup>1.1</sup>	-1	
141186	214.920742	52.901108	15931	Filler	27.5±0.1	26.0±2.0	27.0±7.0	12.1 <sub>2.7</sub> <sup>10.0*</sup>	-1	
46784	214.969498	52.927092	10621	Filler	27.07±0.04	27.64±0.04	27.56±0.04	1.0 <sub>1.3</sub> <sup>1.8</sup>	-1	
21020	214.888957	52.884764	10037	Filler	27.0±0.2	26.98±0.04	27.61±0.06	0.4 <sub>0.25</sub> <sup>0.46</sup>	-1	
31210	214.915047	52.948342	10621	Contaminant	27.01±0.03	27.52±0.03	27.7±0.04	2.0 <sub>1.7</sub> <sup>2.1</sup>	-1	
112432	214.965906	52.933838	15931	Filler	27.55±0.06	27.67±0.04	27.79±0.06	0.0 <sub>0.91</sub> <sup>1.9</sup>	-1	
112876	214.900136	52.886169	30111	Filler	27.77±0.06	27.74±0.03	27.85±0.04	1.0 <sub>0.97</sub> <sup>1.7</sup>	-1	
104864	214.831294	52.856964	15056	Filler	-1	28.6±0.2	27.9±0.1	15.7 <sub>9.3</sub> <sup>20.0</sup>	-1	
104854	214.841842	52.864873	15056	Filler	27.54±0.04	27.78±0.03	27.91±0.04	2.0 <sub>1.8</sub> <sup>2.4</sup>	-1	
117548	214.944021	52.903844	15931	Filler	28.4±0.2	28.52±0.09	27.97±0.09	6.0 <sub>4.6</sub> <sup>7.4</sup>	-1	
84860	214.902185	52.848443	30111	Filler	26.64±0.05	28.0±0.1	28.0±0.1	6.0 <sub>6.0</sub> <sup>6.4</sup>	-1	
101330	214.932228	52.938464	15931	Filler	27.8±0.1	27.91±0.08	28.02±0.06	6.0 <sub>5.1</sub> <sup>6.2</sup>	-1	
94028	214.82841	52.883933	15056	Filler	28.2±0.1	28.07±0.06	28.04±0.06	6.0 <sub>1.4</sub> <sup>6.1</sup>	-1	
86451	214.972369	52.902641	15931	Filler	28.7±0.2	28.8±0.08	28.15±0.07	8.0 <sub>5.8</sub> <sup>8.6</sup>	-1	
82490	214.998193	52.909699	15931	Filler	28.21±0.07	27.9±0.03	28.16±0.05	1.0 <sub>1.0</sub> <sup>1.5</sup>	-1	

**Table 4** continued

Table 4 (continued)

THRILS ID <sub>MPT</sub>	Coordinates		THRILS		Magnitudes			Prior Redshifts	
	RA	DEC	ExpTime [s]	Category	H	3.60	4.50	$z_{phot}$	$z_{spec}$
100820	214.855425	52.885063	30111	Primary	28.0±0.1	28.8±0.1	28.25±0.07	9.8 <sup>10.0</sup> <sub>9.0</sub>	-1
104352	214.950295	52.942885	15931	Filler	29.0±0.2	29.3±0.1	28.34±0.07	8.0 <sup>7.6</sup> <sub>7.2</sub>	-1
123654	214.973961	52.905454	31862	Filler	31.0±1.0	30.4±0.4	28.35±0.09	14.7 <sup>20.0</sup> <sub>10.0</sub>	-1
119258	214.881119	52.853086	20074	Contaminant	27.48±0.06	28.31±0.07	28.38±0.08	0.0 <sup>3.2</sup> <sub>0.25</sub>	-1
115974	214.969318	52.925426	10621	Contaminant	28.0±0.1	28.7±0.2	28.4±0.2	6.0 <sup>8.0</sup> <sub>2.6</sub>	-1
86348	214.916438	52.862712	20074	Contaminant	28.2±0.2	28.3±0.1	28.4±0.2	0.2 <sup>10.0</sup> <sub>1.2</sub>	-1
87467	214.886685	52.844783	15056	Filler	28.28±0.09	28.13±0.05	28.51±0.07	5.0 <sup>4.9</sup> <sub>0.88</sub>	-1
116137	214.857639	52.849729	15056	Filler	27.0±-1.0	27.81±0.08	28.6±0.2	4.8 <sup>10.0</sup> <sub>1.2</sub>	-1
81605	215.001818	52.909548	15931	Filler	28.54±0.07	28.53±0.04	28.69±0.06	2.0 <sup>2.7</sup> <sub>1.9</sub>	-1
123181	214.96947	52.926907	15931	Filler	28.0±-1.0	-1	28.8±0.1	9.8 <sup>10.0</sup> <sub>8.8</sub>	-1
123813	214.976084	52.900459	15931	Filler	-1	-1	28.8±0.08	9.8 <sup>10.0</sup> <sub>9.7</sub>	-1
113467	214.904735	52.887273	15056	Filler	28.8±0.2	28.56±0.06	28.8±0.08	0.0 <sup>2.1</sup> <sub>0.76</sub>	-1
114210	214.945117	52.913788	15931	Filler	27.9±0.1	28.09±0.09	28.8±0.2	7.0 <sup>8.2</sup> <sub>1.8</sub>	-1
84761	214.902143	52.848134	10037	Contaminant	28.8±0.2	28.6±0.1	28.8±0.2	6.0 <sup>6.3</sup> <sub>1.6</sub>	-1
119213	214.94987	52.901436	15931	Filler	29.0±0.1	29.01±0.06	28.85±0.08	8.0 <sup>8.6</sup> <sub>1.7</sub>	-1
101212	214.932314	52.938602	10621	Filler	28.3±0.1	28.62±0.09	28.9±0.1	0.0 <sup>3.1</sup> <sub>0.31</sub>	-1
86560	214.971243	52.902124	15931	Filler	28.0±-1.0	27.6±0.1	28.9±0.5	19.3 <sup>20.0</sup> <sub>4.2</sub>	-1
114558	214.97158	52.931663	15931	Filler	29.2±0.4	28.2±0.1	28.9±0.3	7.0 <sup>6.9</sup> <sub>5.6</sub>	-1
97545	214.855401	52.893852	10037	Contaminant	29.4±0.2	28.61±0.06	28.95±0.07	5.0 <sup>5.8</sup> <sub>3.7</sub>	-1
150502	214.984105	52.912764	15931	Filler	27.42±0.07	-1	29.0±7.0	12.1 <sup>10.0*</sup> <sub>10.0</sub>	-1
105717	214.887338	52.894826	15056	Filler	30.4±0.5	29.6±0.2	29.02±0.08	15.3 <sup>20.0</sup> <sub>3.3</sub>	-1
123426	214.949958	52.899793	15931	Filler	33.0±5.0	30.7±0.2	29.04±0.09	15.3 <sup>20.0</sup> <sub>7.5</sub>	-1
123055	214.860476	52.854767	20074	Contaminant	31.0±1.0	29.1±0.1	29.1±0.1	4.0 <sup>20.0</sup> <sub>3.0</sub>	-1
97782	214.911942	52.933363	15931	Filler	28.3±0.3	28.6±0.2	29.1±0.3	9.4 <sup>20.0</sup> <sub>4.2</sub>	-1
123620	214.962746	52.897695	15931	Filler	-1	30.7±0.3	29.1±0.1	15.8 <sup>20.0</sup> <sub>7.8</sub>	-1
82395	214.910708	52.847336	10037	Filler	29.1±0.1	29.17±0.09	29.3±0.1	1.0 <sup>5.3</sup> <sub>1.2</sub>	-1
107965	214.834643	52.850082	15056	Filler	-1	29.1±0.2	29.3±0.3	16.9 <sup>20.0</sup> <sub>4.4</sub>	-1
123630	214.973897	52.905182	10621	Contaminant	29.0±-1.0	-1	29.4±0.1	9.8 <sup>10.0</sup> <sub>8.9</sub>	-1
116741	214.888132	52.8666	5019	Contaminant	29.9±0.2	29.7±0.1	29.43±0.07	6.0 <sup>6.3</sup> <sub>3.0</sub>	-1
125652	214.888834	52.884585	15056	Filler	-1	30.5±0.3	29.4±0.1	17.6 <sup>20.0</sup> <sub>8.7</sub>	-1
117080	214.944081	52.904108	5310	Contaminant	30.1±0.3	29.38±0.06	29.5±0.1	4.0 <sup>6.8</sup> <sub>3.8</sub>	-1
88081	214.977307	52.913208	10621	Contaminant	30.0±0.3	29.6±0.1	29.6±0.2	6.0 <sup>6.7</sup> <sub>2.1</sub>	-1
84338	214.968669	52.894157	15931	Filler	31.0±-1.0	28.81±0.08	29.7±0.3	13.7 <sup>10.0</sup> <sub>10.0</sub>	-1
105649	214.887413	52.895097	5019	Contaminant	29.1±0.1	29.9±0.1	29.8±0.1	1.0 <sup>4.2</sup> <sub>1.1</sub>	-1
93662	214.888977	52.895245	10037	Filler	29.0±0.1	29.6±0.1	29.8±0.1	0.5 <sup>0.82</sup> <sub>0.28</sub>	-1
106298	214.845606	52.863064	15056	Filler	31.0±2.0	29.1±0.1	30.0±0.4	15.5 <sup>20.0</sup> <sub>10.0</sub>	-1
105874	214.891941	52.897584	15056	Filler	31.0±2.0	29.0±0.1	30.0±0.3	4.0 <sup>4.5</sup> <sub>0.67</sub>	-1
102778	214.880983	52.898025	15056	Filler	29.4±0.3	28.9±0.1	30.2±0.3	1.0 <sup>4.6</sup> <sub>0.55</sub>	-1
106725	214.841309	52.858729	15056	Filler	29.0±0.3	28.4±0.1	30.2±0.6	7.0 <sup>7.7</sup> <sub>1.9</sub>	-1
106752	214.841367	52.858767	10037	Filler	29.1±0.2	30.6±0.5	30.2±0.4	7.0 <sup>9.1</sup> <sub>6.1</sub>	-1

Table 4 continued

Table 4 (continued)

THRILS ID <sub>MPT</sub>	Coordinates		THRILS		Magnitudes			Prior Redshifts	
	RA	DEC	ExpTime [s]	Category	H	3.60	4.50	$z_{phot}$	$z_{spec}$
87731	214.968843	52.944907	15931	Filler	30.1±0.4	29.7±0.1	30.6±0.4	5.0 <sup>5.4</sup> <sub>1.3</sub>	-1
105221	214.936107	52.930431	5310	Contaminant	30.1±0.2	30.7±0.1	31.4±0.2	0.0 <sup>3.1</sup> <sub>0.13</sub>	-1
120077	214.89006	52.85531	15056	Filler	27.6±0.1	27.92±0.09	31.0±3.0	4.0 <sup>4.5</sup> <sub>0.64</sub>	-1
106646	214.838367	52.856751	15056	Filler	-1	28.41±0.08	32.0±3.0	19.2 <sup>20.0</sup> <sub>10.0</sub>	-1

NOTE—Table of the 81 non-detections in the THRILS data sorted in order of brightness in three filters (in descending wavelength order). Sources that are not detected or do not have data in a certain filter are assigned a value of -1 for that magnitude. Description of Columns: 1) ID in the THRILS MPT, 2-3) Coordinates, 4-5) Exposure time and target category for the source as described in §2.2, 6-8) Magnitude of the source in 3 representative bands as described in §2.1, 9-10) Prior measurements of  $z_{phot}$  and  $z_{spec}$  from ancillary data as described in §2.1.

\* Sources with *HST* only derived  $z_{phot}$  measurements as they do not have *JWST*/NIRCam coverage.

<sup>a</sup> DJA (A. de Graaff et al. 2024; K. E. Heintz et al. 2024).

<sup>b</sup> CANDELS DEEP2 (M. Stefanon et al. 2017).

## REFERENCES

- Adams, N. J., Conselice, C. J., Ferreira, L., et al. 2022, arXiv e-prints, arXiv:2207.11217.  
<https://arxiv.org/abs/2207.11217>
- Akins, H. B., Casey, C. M., Lambrides, E., et al. 2025, ApJ, 991, 37, doi: [10.3847/1538-4357/ade984](https://doi.org/10.3847/1538-4357/ade984)
- Ananna, T. T., Bogdán, Á., Kovács, O. E., Natarajan, P., & Hickox, R. C. 2024, ApJL, 969, L18, doi: [10.3847/2041-8213/ad5669](https://doi.org/10.3847/2041-8213/ad5669)
- Arrabal Haro, P., Dickinson, M., Finkelstein, S. L., et al. 2023a, Nature, 622, 707, doi: [10.1038/s41586-023-06521-7](https://doi.org/10.1038/s41586-023-06521-7)
- Arrabal Haro, P., Dickinson, M., Finkelstein, S. L., et al. 2023b, ApJL, 951, L22, doi: [10.3847/2041-8213/acdd54](https://doi.org/10.3847/2041-8213/acdd54)
- Astropy Collaboration, Robitaille, T. P., Tollerud, E. J., et al. 2013, A&A, 558, A33, doi: [10.1051/0004-6361/201322068](https://doi.org/10.1051/0004-6361/201322068)
- Astropy Collaboration, Price-Whelan, A. M., Sipőcz, B. M., et al. 2018, AJ, 156, 123, doi: [10.3847/1538-3881/aabc4f](https://doi.org/10.3847/1538-3881/aabc4f)
- Astropy Collaboration, Price-Whelan, A. M., Lim, P. L., et al. 2022, ApJ, 935, 167, doi: [10.3847/1538-4357/ac7c74](https://doi.org/10.3847/1538-4357/ac7c74)
- Atek, H., Shuntov, M., Furtak, L. J., et al. 2023, MNRAS, 519, 1201, doi: [10.1093/mnras/stac3144](https://doi.org/10.1093/mnras/stac3144)
- Backhaus, B. E., Kirkpatrick, A., Yang, G., et al. 2025, arXiv e-prints, arXiv:2503.19078, doi: [10.48550/arXiv.2503.19078](https://doi.org/10.48550/arXiv.2503.19078)
- Bagley, M. B., Finkelstein, S. L., Koekemoer, A. M., et al. 2022, arXiv e-prints, arXiv:2211.02495.  
<https://arxiv.org/abs/2211.02495>
- Balogh, M. L., Morris, S. L., Yee, H. K. C., Carlberg, R. G., & Ellingson, E. 1999, ApJ, 527, 54, doi: [10.1086/308056](https://doi.org/10.1086/308056)
- Barro, G., Perez-Gonzalez, P. G., Kocevski, D. D., et al. 2024a, arXiv e-prints, arXiv:2412.01887, doi: [10.48550/arXiv.2412.01887](https://doi.org/10.48550/arXiv.2412.01887)
- Barro, G., Pérez-González, P. G., Kocevski, D. D., et al. 2024b, ApJ, 963, 128, doi: [10.3847/1538-4357/ad167e](https://doi.org/10.3847/1538-4357/ad167e)
- Berg, D. A., Chisholm, J., Erb, D. K., et al. 2019, ApJL, 878, L3, doi: [10.3847/2041-8213/ab21dc](https://doi.org/10.3847/2041-8213/ab21dc)
- Berg, D. A., Chisholm, J., Erb, D. K., et al. 2021, ApJ, 922, 170, doi: [10.3847/1538-4357/ac141b](https://doi.org/10.3847/1538-4357/ac141b)
- Bertin, E., & Arnouts, S. 1996, A&AS, 117, 393, doi: [10.1051/aas:1996164](https://doi.org/10.1051/aas:1996164)
- Böker, T., Beck, T. L., Birkmann, S. M., et al. 2023, PASP, 135, 038001, doi: [10.1088/1538-3873/acb846](https://doi.org/10.1088/1538-3873/acb846)
- Boylan-Kolchin, M. 2022, arXiv e-prints, arXiv:2208.01611.  
<https://arxiv.org/abs/2208.01611>
- Brammer, G. B., Sánchez-Janssen, R., Labbé, I., et al. 2012, ApJL, 758, L17, doi: [10.1088/2041-8205/758/1/L17](https://doi.org/10.1088/2041-8205/758/1/L17)
- Bromm, V. 2013, Reports on Progress in Physics, 76, 112901, doi: [10.1088/0034-4885/76/11/112901](https://doi.org/10.1088/0034-4885/76/11/112901)
- Bromm, V., Ferrara, A., Coppi, P. S., & Larson, R. B. 2001a, MNRAS, 328, 969, doi: [10.1046/j.1365-8711.2001.04915.x](https://doi.org/10.1046/j.1365-8711.2001.04915.x)
- Bromm, V., Kudritzki, R. P., & Loeb, A. 2001b, ApJ, 552, 464
- Bromm, V., & Loeb, A. 2003, Nature, 425, 812, doi: [10.1038/nature02071](https://doi.org/10.1038/nature02071)
- Bromm, V., & Yoshida, N. 2011, ARA&A, 49, 373, doi: [10.1146/annurev-astro-081710-102608](https://doi.org/10.1146/annurev-astro-081710-102608)
- Bushouse, H., Eisenhamer, J., Dencheva, N., et al. 2022, JWST Calibration Pipeline, 1.8.5 Zenodo, doi: [10.5281/zenodo.7429939](https://doi.org/10.5281/zenodo.7429939)
- Carnall, A. C., Leja, J., Johnson, B. D., et al. 2019, The Astrophysical Journal, 873, 44, doi: [10.3847/1538-4357/ab04a2](https://doi.org/10.3847/1538-4357/ab04a2)
- Carnall, A. C., McLure, R. J., Dunlop, J. S., et al. 2023a, Nature, 619, 716, doi: [10.1038/s41586-023-06158-6](https://doi.org/10.1038/s41586-023-06158-6)
- Carnall, A. C., McLure, R. J., Dunlop, J. S., et al. 2023b, Nature, 619, 716, doi: [10.1038/s41586-023-06158-6](https://doi.org/10.1038/s41586-023-06158-6)
- Carnall, A. C., Cullen, F., McLure, R. J., et al. 2024, MNRAS, 534, 325, doi: [10.1093/mnras/stae2092](https://doi.org/10.1093/mnras/stae2092)
- Casey, C. M., Akins, H. B., Kokorev, V., et al. 2024, ApJL, 975, L4, doi: [10.3847/2041-8213/ad7ba7](https://doi.org/10.3847/2041-8213/ad7ba7)
- Chabrier, G. 2003, PASP, 115, 763
- Chisholm, J., Berg, D. A., Endsley, R., et al. 2024, MNRAS, 534, 2633, doi: [10.1093/mnras/stae2199](https://doi.org/10.1093/mnras/stae2199)
- Chon, S., Omukai, K., & Schneider, R. 2021, MNRAS, 508, 4175, doi: [10.1093/mnras/stab2497](https://doi.org/10.1093/mnras/stab2497)
- Chworowsky, K., Finkelstein, S. L., Spilker, J. S., et al. 2023, ApJ, 951, 49, doi: [10.3847/1538-4357/acd1e3](https://doi.org/10.3847/1538-4357/acd1e3)
- Chworowsky, K., Finkelstein, S. L., Boylan-Kolchin, M., et al. 2024, AJ, 168, 113, doi: [10.3847/1538-3881/ad57c1](https://doi.org/10.3847/1538-3881/ad57c1)
- Clarke, C. J., & Bromm, V. 2003, MNRAS, 343, 1224, doi: [10.1046/j.1365-8711.2003.06765.x](https://doi.org/10.1046/j.1365-8711.2003.06765.x)
- Cleri, N. J., Yang, G., Papovich, C., et al. 2023a, ApJ, 948, 112, doi: [10.3847/1538-4357/acc1e6](https://doi.org/10.3847/1538-4357/acc1e6)
- Cleri, N. J., Olivier, G. M., Hutchison, T. A., et al. 2023b, ApJ, 953, 10, doi: [10.3847/1538-4357/acde55](https://doi.org/10.3847/1538-4357/acde55)
- Cleri, N. J., Olivier, G. M., Backhaus, B. E., et al. 2025, arXiv e-prints, arXiv:2506.21660, doi: [10.48550/arXiv.2506.21660](https://doi.org/10.48550/arXiv.2506.21660)
- Covelo-Paz, A., Meuwly, C., Oesch, P. A., et al. 2025, arXiv e-prints, arXiv:2506.22540, doi: [10.48550/arXiv.2506.22540](https://doi.org/10.48550/arXiv.2506.22540)
- Cox, I. G., Kartaltepe, J. S., Bagley, M. B., et al. 2025, arXiv e-prints, arXiv:2510.08743, doi: [10.48550/arXiv.2510.08743](https://doi.org/10.48550/arXiv.2510.08743)

- Cueto, E. R., Hutter, A., Dayal, P., et al. 2024, *A&A*, 686, A138, doi: [10.1051/0004-6361/202349017](https://doi.org/10.1051/0004-6361/202349017)
- Curtis-Lake, E., Carniani, S., Cameron, A., et al. 2023, *Nature Astronomy*, 7, 622, doi: [10.1038/s41550-023-01918-w](https://doi.org/10.1038/s41550-023-01918-w)
- Davis, K., Trump, J. R., Simons, R. C., et al. 2024, *ApJ*, 974, 42, doi: [10.3847/1538-4357/ad6865](https://doi.org/10.3847/1538-4357/ad6865)
- de Graaff, A., Rix, H.-W., Carniani, S., et al. 2024, *A&A*, 684, A87, doi: [10.1051/0004-6361/202347755](https://doi.org/10.1051/0004-6361/202347755)
- de Graaff, A., Brammer, G., Weibel, A., et al. 2025, *A&A*, 697, A189, doi: [10.1051/0004-6361/202452186](https://doi.org/10.1051/0004-6361/202452186)
- Donnan, C. T., McLeod, D. J., Dunlop, J. S., et al. 2022, arXiv e-prints, arXiv:2207.12356. <https://arxiv.org/abs/2207.12356>
- Endsley, R., Chisholm, J., Stark, D. P., Topping, M. W., & Whitler, L. 2025, *The Astrophysical Journal*, 987, 189, doi: [10.3847/1538-4357/adde74](https://doi.org/10.3847/1538-4357/adde74)
- Euclid Collaboration, Navarro-Carrera, R., Caputi, K. I., et al. 2025, arXiv e-prints, arXiv:2511.11943, doi: [10.48550/arXiv.2511.11943](https://doi.org/10.48550/arXiv.2511.11943)
- Ferland, G. J., Porter, R. L., van Hoof, P. A. M., et al. 2013, *RMxAA*, 49, 137. <https://arxiv.org/abs/1302.4485>
- Ferrara, A., Pallottini, A., & Dayal, P. 2023, *MNRAS*, 522, 3986, doi: [10.1093/mnras/stad1095](https://doi.org/10.1093/mnras/stad1095)
- Finkelstein, S. L., Bagley, M. B., Arrabal Haro, P., et al. 2022a, arXiv e-prints, arXiv:2207.12474. <https://arxiv.org/abs/2207.12474>
- Finkelstein, S. L., Bagley, M. B., Ferguson, H. C., et al. 2022b, arXiv e-prints, arXiv:2211.05792. <https://arxiv.org/abs/2211.05792>
- Finkelstein, S. L., Bagley, M., Song, M., et al. 2022c, *ApJ*, 928, 52, doi: [10.3847/1538-4357/ac3aed](https://doi.org/10.3847/1538-4357/ac3aed)
- Finkelstein, S. L., Leung, G. C. K., Bagley, M. B., et al. 2024, *ApJL*, 969, L2, doi: [10.3847/2041-8213/ad4495](https://doi.org/10.3847/2041-8213/ad4495)
- Finkelstein, S. L., Bagley, M. B., Arrabal Haro, P., et al. 2025, *ApJL*, 983, L4, doi: [10.3847/2041-8213/adbbd3](https://doi.org/10.3847/2041-8213/adbbd3)
- Fujimoto, S., Arrabal Haro, P., Dickinson, M., et al. 2023, arXiv e-prints, arXiv:2301.09482. <https://arxiv.org/abs/2301.09482>
- Furtak, L. J., Labbé, I., Zitrin, A., et al. 2024, *Nature*, 628, 57, doi: [10.1038/s41586-024-07184-8](https://doi.org/10.1038/s41586-024-07184-8)
- Gardner, J. P., Mather, J. C., Abbott, R., et al. 2023, *PASP*, 135, 068001, doi: [10.1088/1538-3873/acd1b5](https://doi.org/10.1088/1538-3873/acd1b5)
- Glazebrook, K., Nanayakkara, T., Schreiber, C., et al. 2024, *Nature*, 628, 277, doi: [10.1038/s41586-024-07191-9](https://doi.org/10.1038/s41586-024-07191-9)
- Gloude-mans, A. J., Duncan, K. J., Eilers, A.-C., et al. 2025, *ApJ*, 986, 130, doi: [10.3847/1538-4357/adddb9](https://doi.org/10.3847/1538-4357/adddb9)
- Greene, J. E., Labbe, I., Goulding, A. D., et al. 2023, arXiv e-prints, arXiv:2309.05714, doi: [10.48550/arXiv.2309.05714](https://doi.org/10.48550/arXiv.2309.05714)
- Grogin, N. A., Kocevski, D. D., Faber, S. M., et al. 2011, *ApJS*, 197, 35. <https://arxiv.org/abs/1105.3753>
- Harikane, Y., Ouchi, M., Oguri, M., et al. 2022, arXiv e-prints, arXiv:2208.01612. <https://arxiv.org/abs/2208.01612>
- Harikane, Y., Zhang, Y., Nakajima, K., et al. 2023, *ApJ*, 959, 39, doi: [10.3847/1538-4357/ad029e](https://doi.org/10.3847/1538-4357/ad029e)
- Heintz, K. E., Watson, D., Brammer, G., et al. 2024, *Science*, 384, 890, doi: [10.1126/science.adj0343](https://doi.org/10.1126/science.adj0343)
- Hinshaw, G., Larson, D., Komatsu, E., et al. 2013, *ApJS*, 208, 19, doi: [10.1088/0067-0049/208/2/19](https://doi.org/10.1088/0067-0049/208/2/19)
- Horne, K. 1986, *PASP*, 98, 609, doi: [10.1086/131801](https://doi.org/10.1086/131801)
- Hviding, R. E., de Graaff, A., Miller, T. B., et al. 2025, *A&A*, 702, A57, doi: [10.1051/0004-6361/202555816](https://doi.org/10.1051/0004-6361/202555816)
- Inayoshi, K. 2025, *ApJL*, 988, L22, doi: [10.3847/2041-8213/adea66](https://doi.org/10.3847/2041-8213/adea66)
- Iverson, R. J., Chapman, S. C., Faber, S. M., et al. 2007, *ApJL*, 660, L77, doi: [10.1086/517917](https://doi.org/10.1086/517917)
- Iyer, K. G., Gawiser, E., Faber, S. M., et al. 2021, dense\_basis: Dense Basis SED fitting,, Astrophysics Source Code Library, record ascl:2104.015
- Jaacks, J., Thompson, R., Finkelstein, S. L., & Bromm, V. 2018, *MNRAS*, 475, 4396. <https://arxiv.org/abs/1705.08059>
- Jung, I., Finkelstein, S. L., Livermore, R. C., et al. 2018, *ApJ*, 864, 103. <https://arxiv.org/abs/1803.01870>
- Jung, I., Finkelstein, S. L., Larson, R. L., et al. 2022, arXiv e-prints, arXiv:2212.09850, doi: [10.48550/arXiv.2212.09850](https://doi.org/10.48550/arXiv.2212.09850)
- Juodžbalis, I., Maiolino, R., Baker, W. M., et al. 2024, *Nature*, 636, 594, doi: [10.1038/s41586-024-08210-5](https://doi.org/10.1038/s41586-024-08210-5)
- Kewley, L. J., Nicholls, D. C., & Sutherland, R. S. 2019, *ARA&A*, 57, 511, doi: [10.1146/annurev-astro-081817-051832](https://doi.org/10.1146/annurev-astro-081817-051832)
- King, A. 2024, *MNRAS*, 531, 550, doi: [10.1093/mnras/stae1171](https://doi.org/10.1093/mnras/stae1171)
- Klessen, R. S., & Glover, S. C. O. 2023, *ARA&A*, 61, 65, doi: [10.1146/annurev-astro-071221-053453](https://doi.org/10.1146/annurev-astro-071221-053453)
- Kocevski, D., Onoue, M., Inayoshi, K., & Trump, J. 2023, *ApJL* Submitted
- Kocevski, D. D., Barro, G., McGrath, E. J., et al. 2022, arXiv e-prints, arXiv
- Kodra, D., Andrews, B. H., Newman, J. A., et al. 2023, *ApJ*, 942, 36, doi: [10.3847/1538-4357/ac9f12](https://doi.org/10.3847/1538-4357/ac9f12)
- Koekemoer, A. M., Faber, S. M., Ferguson, H. C., et al. 2011, *ApJS*, 197, 36. <https://arxiv.org/abs/1105.3754>
- Kokorev, V., Fujimoto, S., Labbe, I., et al. 2023, *ApJL*, 957, L7, doi: [10.3847/2041-8213/ad037a](https://doi.org/10.3847/2041-8213/ad037a)
- Kokorev, V., Chisholm, J., Endsley, R., et al. 2024a, *ApJ*, 975, 178, doi: [10.3847/1538-4357/ad7d03](https://doi.org/10.3847/1538-4357/ad7d03)

- Kokorev, V., Chisholm, J., Endsley, R., et al. 2024b, *ApJ*, 975, 178, doi: [10.3847/1538-4357/ad7d03](https://doi.org/10.3847/1538-4357/ad7d03)
- Kroupa, P., Weidner, C., Pflamm-Altenburg, J., et al. 2013, in *Planets, Stars and Stellar Systems. Volume 5: Galactic Structure and Stellar Populations*, ed. T. D. Oswalt & G. Gilmore, Vol. 5, 115, doi: [10.1007/978-94-007-5612-0\\_4](https://doi.org/10.1007/978-94-007-5612-0_4)
- Labbe, I., van Dokkum, P., Nelson, E., et al. 2022, arXiv e-prints, arXiv:2207.12446, <https://arxiv.org/abs/2207.12446>
- Lambrides, E., Garofali, K., Larson, R., et al. 2024, arXiv e-prints, arXiv:2409.13047, doi: [10.48550/arXiv.2409.13047](https://doi.org/10.48550/arXiv.2409.13047)
- Lambrides, E., Larson, R., Hutchison, T., et al. 2025, arXiv e-prints, arXiv:2509.09607, doi: [10.48550/arXiv.2509.09607](https://doi.org/10.48550/arXiv.2509.09607)
- Landsman, W. B. 1993, in *Astronomical Society of the Pacific Conference Series*, Vol. 52, *Astronomical Data Analysis Software and Systems II*, ed. R. J. Hanisch, R. J. V. Brissenden, & J. Barnes, 246
- Larson, R. B. 1998, *MNRAS*, 301, 569, doi: [10.1046/j.1365-8711.1998.02045.x](https://doi.org/10.1046/j.1365-8711.1998.02045.x)
- Larson, R. L., Finkelstein, S. L., Pirzkal, N., et al. 2018, *ApJ*, 858, 94. <https://arxiv.org/abs/1712.05807>
- Larson, R. L., Finkelstein, S. L., Hutchison, T. A., et al. 2022a, *ApJ*, 930, 104, doi: [10.3847/1538-4357/ac5dbd](https://doi.org/10.3847/1538-4357/ac5dbd)
- Larson, R. L., Hutchison, T. A., Bagley, M., et al. 2022b, arXiv e-prints, arXiv:2211.10035, doi: [10.48550/arXiv.2211.10035](https://doi.org/10.48550/arXiv.2211.10035)
- Larson, R. L., Finkelstein, S. L., Kocevski, D. D., et al. 2023, *ApJL*, 953, L29, doi: [10.3847/2041-8213/ace619](https://doi.org/10.3847/2041-8213/ace619)
- Leja, J., Carnall, A., Johnson, B., Conroy, C., & Speagle, J. 2019, *The Astrophysical Journal*, 876, 3, doi: [10.3847/1538-4357/ab133c](https://doi.org/10.3847/1538-4357/ab133c)
- Leung, G. C. K., Finkelstein, S. L., Pérez-González, P. G., et al. 2024, arXiv e-prints, arXiv:2411.12005, doi: [10.48550/arXiv.2411.12005](https://doi.org/10.48550/arXiv.2411.12005)
- Liu, B., & Bromm, V. 2020, *MNRAS*, 497, 2839, doi: [10.1093/mnras/staa2143](https://doi.org/10.1093/mnras/staa2143)
- Looser, T. J., D'Eugenio, F., Maiolino, R., et al. 2023, arXiv e-prints, arXiv:2306.02470, doi: [10.48550/arXiv.2306.02470](https://doi.org/10.48550/arXiv.2306.02470)
- Lovell, C. C., Harrison, I., Harikane, Y., Tacchella, S., & Wilkins, S. M. 2023, *MNRAS*, 518, 2511, doi: [10.1093/mnras/stac3224](https://doi.org/10.1093/mnras/stac3224)
- Lupi, A., Trinca, A., Volonteri, M., Dotti, M., & Mazzucchelli, C. 2024, *A&A*, 689, A128, doi: [10.1051/0004-6361/202451249](https://doi.org/10.1051/0004-6361/202451249)
- Madau, P., & Haardt, F. 2024a, *ApJL*, 976, L24, doi: [10.3847/2041-8213/ad90e1](https://doi.org/10.3847/2041-8213/ad90e1)
- Madau, P., & Haardt, F. 2024b, *ApJL*, 976, L24, doi: [10.3847/2041-8213/ad90e1](https://doi.org/10.3847/2041-8213/ad90e1)
- Maiolino, R., Uebler, H., Perna, M., et al. 2023, arXiv e-prints, arXiv:2306.00953, doi: [10.48550/arXiv.2306.00953](https://doi.org/10.48550/arXiv.2306.00953)
- Mansheim, A. S., Lemaux, B. C., Tomczak, A. R., et al. 2017, *MNRAS*, 469, L20, doi: [10.1093/mnrasl/slx041](https://doi.org/10.1093/mnrasl/slx041)
- Matthee, J. 2025, arXiv e-prints, arXiv:2511.04843, doi: [10.48550/arXiv.2511.04843](https://doi.org/10.48550/arXiv.2511.04843)
- Matthee, J., Naidu, R. P., Brammer, G., et al. 2024, *ApJ*, 963, 129, doi: [10.3847/1538-4357/ad2345](https://doi.org/10.3847/1538-4357/ad2345)
- Naidu, R. P., Oesch, P. A., Brammer, G., et al. 2025a, arXiv e-prints, arXiv:2505.11263, doi: [10.48550/arXiv.2505.11263](https://doi.org/10.48550/arXiv.2505.11263)
- Naidu, R. P., Matthee, J., Katz, H., et al. 2025b, arXiv e-prints, arXiv:2503.16596, doi: [10.48550/arXiv.2503.16596](https://doi.org/10.48550/arXiv.2503.16596)
- Nakajima, K., & Maiolino, R. 2022, *MNRAS*, 513, 5134, doi: [10.1093/mnras/stac1242](https://doi.org/10.1093/mnras/stac1242)
- Nandra, K., Laird, E. S., Aird, J. A., et al. 2015, *ApJS*, 220, 10, doi: [10.1088/0067-0049/220/1/10](https://doi.org/10.1088/0067-0049/220/1/10)
- Olivier, G. M., Berg, D. A., Chisholm, J., et al. 2022, *ApJ*, 938, 16, doi: [10.3847/1538-4357/ac8f2c](https://doi.org/10.3847/1538-4357/ac8f2c)
- Pacucci, F., & Narayan, R. 2024, *ApJ*, 976, 96, doi: [10.3847/1538-4357/ad84f7](https://doi.org/10.3847/1538-4357/ad84f7)
- Park, S. Q., Barnby, P., Willner, S. P., et al. 2010, *ApJ*, 717, 1181, doi: [10.1088/0004-637X/717/2/1181](https://doi.org/10.1088/0004-637X/717/2/1181)
- Pawlik, A. H., Milosavljević, M., & Bromm, V. 2011, *ApJ*, 731, 54, doi: [10.1088/0004-637X/731/1/54](https://doi.org/10.1088/0004-637X/731/1/54)
- Pérez-González, P. G., Costantin, L., Langeroodi, D., et al. 2023, *ApJL*, 951, L1, doi: [10.3847/2041-8213/acd9d0](https://doi.org/10.3847/2041-8213/acd9d0)
- Pérez-González, P. G., Barro, G., Rieke, G. H., et al. 2024a, *ApJ*, 968, 4, doi: [10.3847/1538-4357/ad38bb](https://doi.org/10.3847/1538-4357/ad38bb)
- Pérez-González, P. G., Barro, G., Rieke, G. H., et al. 2024b, *ApJ*, 968, 4, doi: [10.3847/1538-4357/ad38bb](https://doi.org/10.3847/1538-4357/ad38bb)
- Pérez-González, P. G., D'Eugenio, F., Rodríguez del Pino, B., et al. 2025, *Nature Astronomy*, 9, 1240, doi: [10.1038/s41550-025-02586-8](https://doi.org/10.1038/s41550-025-02586-8)
- Pérez-González, P. G., Östlin, G., Costantin, L., et al. 2025b, *ApJ*, 991, 179, doi: [10.3847/1538-4357/adf8c9](https://doi.org/10.3847/1538-4357/adf8c9)
- Pirzkal, N., Malhotra, S., Ryan, R. E., et al. 2017, *ApJ*, 846, 84. <https://arxiv.org/abs/1706.02669>
- Poggianti, B. M., Smail, I., Dressler, A., et al. 1999, *ApJ*, 518, 576, doi: [10.1086/307322](https://doi.org/10.1086/307322)
- Poggianti, B. M., Aragón-Salamanca, A., Zaritsky, D., et al. 2009, *ApJ*, 693, 112, doi: [10.1088/0004-637X/693/1/112](https://doi.org/10.1088/0004-637X/693/1/112)
- Raiter, A., Schaerer, D., & Fosbury, R. A. E. 2010, *A&A*, 523, A64, doi: [10.1051/0004-6361/201015236](https://doi.org/10.1051/0004-6361/201015236)

- Ronayne, K., Papovich, C., Kirkpatrick, A., et al. 2025, arXiv e-prints, arXiv:2508.20177, doi: [10.48550/arXiv.2508.20177](https://doi.org/10.48550/arXiv.2508.20177)
- Sanders, R. L., Jones, T., Shapley, A. E., et al. 2020, ApJL, 888, L11, doi: [10.3847/2041-8213/ab5d40](https://doi.org/10.3847/2041-8213/ab5d40)
- Sanders, R. L., Shapley, A. E., Jones, T., et al. 2021, ApJ, 914, 19, doi: [10.3847/1538-4357/abf4c1](https://doi.org/10.3847/1538-4357/abf4c1)
- Schaerer, D. 2003, A&A, 397, 527, doi: [10.1051/0004-6361:20021525](https://doi.org/10.1051/0004-6361:20021525)
- Schneider, R., Ferrara, A., Natarajan, P., & Omukai, K. 2002, ApJ, 571, 30, doi: [10.1086/339917](https://doi.org/10.1086/339917)
- Schneider, R., & Omukai, K. 2010, MNRAS, 402, 429, doi: [10.1111/j.1365-2966.2009.15891.x](https://doi.org/10.1111/j.1365-2966.2009.15891.x)
- Setton, D. J., Greene, J. E., Spilker, J. S., et al. 2025, ApJL, 991, L10, doi: [10.3847/2041-8213/ade78b](https://doi.org/10.3847/2041-8213/ade78b)
- Shapley, A. E., Sanders, R. L., Topping, M. W., et al. 2025, ApJ, 980, 242, doi: [10.3847/1538-4357/adad68](https://doi.org/10.3847/1538-4357/adad68)
- Sharda, P., & Krumholz, M. R. 2022, MNRAS, 509, 1959, doi: [10.1093/mnras/stab2921](https://doi.org/10.1093/mnras/stab2921)
- Smithsonian Astrophysical Observatory. 2000, SAOImage DS9: A utility for displaying astronomical images in the X11 window environment., Astrophysics Source Code Library, record ascl:0003.002 <http://ascl.net/0003.002>
- Stefanon, M., Yan, H., Mobasher, B., et al. 2017, ApJS, 229, 32, doi: [10.3847/1538-4365/aa66cb](https://doi.org/10.3847/1538-4365/aa66cb)
- Steinhardt, C. L., Capak, P., Masters, D., & Speagle, J. S. 2016, ApJ, 824, 21, doi: [10.3847/0004-637X/824/1/21](https://doi.org/10.3847/0004-637X/824/1/21)
- Tang, M., Stark, D. P., Mason, C. A., et al. 2025b, arXiv e-prints, arXiv:2507.08245, doi: [10.48550/arXiv.2507.08245](https://doi.org/10.48550/arXiv.2507.08245)
- Tang, M., Stark, D. P., Topping, M. W., Mason, C., & Ellis, R. S. 2024, ApJ, 975, 208, doi: [10.3847/1538-4357/ad7eb7](https://doi.org/10.3847/1538-4357/ad7eb7)
- Tang, M., Stark, D. P., Chen, Z., et al. 2023, arXiv e-prints, arXiv:2301.07072, doi: [10.48550/arXiv.2301.07072](https://doi.org/10.48550/arXiv.2301.07072)
- Tang, M., Stark, D. P., Plat, A., et al. 2025, ApJ, 991, 217, doi: [10.3847/1538-4357/adfd57](https://doi.org/10.3847/1538-4357/adfd57)
- Taylor, A. J., Finkelstein, S. L., Kocevski, D. D., et al. 2025a, ApJ, 986, 165, doi: [10.3847/1538-4357/add15b](https://doi.org/10.3847/1538-4357/add15b)
- Taylor, A. J., Kokorev, V., Kocevski, D. D., et al. 2025b, ApJL, 989, L7, doi: [10.3847/2041-8213/ade789](https://doi.org/10.3847/2041-8213/ade789)
- Taylor, M. 2011, TOPCAT: Tool for OPERations on Catalogues And Tables., Astrophysics Source Code Library, record ascl:1101.010
- Tilvi, V., Malhotra, S., Rhoads, J. E., et al. 2020, ApJL, 891, L10, doi: [10.3847/2041-8213/ab75ec](https://doi.org/10.3847/2041-8213/ab75ec)
- Urbano Stawinski, S. M., Cooper, M. C., Finkelstein, S. L., et al. 2024, MNRAS, 528, 5624, doi: [10.1093/mnras/stae361](https://doi.org/10.1093/mnras/stae361)
- Valentino, F., Brammer, G., Gould, K. M. L., et al. 2023, ApJ, 947, 20, doi: [10.3847/1538-4357/acbefa](https://doi.org/10.3847/1538-4357/acbefa)
- Venditti, A., Graziani, L., Schneider, R., et al. 2023, MNRAS, 522, 3809, doi: [10.1093/mnras/stad1201](https://doi.org/10.1093/mnras/stad1201)
- Vergani, D., Zamorani, G., Lilly, S., et al. 2010, A&A, 509, A42, doi: [10.1051/0004-6361/200912802](https://doi.org/10.1051/0004-6361/200912802)
- Wang, B., de Graaff, A., Davies, R. L., et al. 2025a, ApJ, 984, 121, doi: [10.3847/1538-4357/adc1ca](https://doi.org/10.3847/1538-4357/adc1ca)
- Wang, B., de Graaff, A., Davies, R. L., et al. 2025b, ApJ, 984, 121, doi: [10.3847/1538-4357/adc1ca](https://doi.org/10.3847/1538-4357/adc1ca)
- Wang, T., Sun, H., Zhou, L., et al. 2025, ApJL, 988, L35, doi: [10.3847/2041-8213/adebe7](https://doi.org/10.3847/2041-8213/adebe7)
- Weaver, J. R., Davidzon, I., Toft, S., et al. 2022, arXiv e-prints, arXiv:2212.02512, doi: [10.48550/arXiv.2212.02512](https://doi.org/10.48550/arXiv.2212.02512)
- Weibel, A., de Graaff, A., Setton, D. J., et al. 2025, ApJ, 983, 11, doi: [10.3847/1538-4357/adab7a](https://doi.org/10.3847/1538-4357/adab7a)
- Whalen, K. E., Weaver, K. A., Hickox, R. C., & Lambrides, E. 2025, arXiv e-prints, arXiv:2509.21236, doi: [10.48550/arXiv.2509.21236](https://doi.org/10.48550/arXiv.2509.21236)
- Whitler, L., Endsley, R., Stark, D. P., et al. 2022, arXiv e-prints, arXiv:2208.01599, <https://arxiv.org/abs/2208.01599>
- Whitler, L., Stark, D. P., Mason, C. A., et al. 2025, arXiv e-prints, arXiv:2510.12019, doi: [10.48550/arXiv.2510.12019](https://doi.org/10.48550/arXiv.2510.12019)
- Williams, C. C., Alberts, S., Ji, Z., et al. 2024, ApJ, 968, 34, doi: [10.3847/1538-4357/ad3f17](https://doi.org/10.3847/1538-4357/ad3f17)
- Xiao, M., Oesch, P. A., Elbaz, D., et al. 2024, Nature, 635, 311, doi: [10.1038/s41586-024-08094-5](https://doi.org/10.1038/s41586-024-08094-5)
- Yang, G., Papovich, C., Bagley, M. B., et al. 2023, ApJL, 956, L12, doi: [10.3847/2041-8213/acfaa0](https://doi.org/10.3847/2041-8213/acfaa0)
- Yue, M., Eilers, A.-C., Ananna, T. T., et al. 2024, ApJL, 974, L26, doi: [10.3847/2041-8213/ad7eba](https://doi.org/10.3847/2041-8213/ad7eba)
- Yung, L. Y. A., Somerville, R. S., Finkelstein, S. L., Wilkins, S. M., & Gardner, J. P. 2024, MNRAS, 527, 5929, doi: [10.1093/mnras/stad3484](https://doi.org/10.1093/mnras/stad3484)
- Zackrisson, E., Rydberg, C.-E., Schaerer, D., Östlin, G., & Tuli, M. 2011, ApJ, 740, 13, doi: [10.1088/0004-637X/740/1/13](https://doi.org/10.1088/0004-637X/740/1/13)
- Zackrisson, E., Hultquist, A., Kordt, A., et al. 2024, MNRAS, 533, 2727, doi: [10.1093/mnras/stae1881](https://doi.org/10.1093/mnras/stae1881)

## All Authors and Affiliations

TAYLOR A. HUTCHISON <sup>1,2,\*</sup> REBECCA L. LARSON <sup>1,3,†</sup> PABLO ARRABAL HARO <sup>2,\*</sup> ERINI LAMBRIDES <sup>2,\*</sup>  
KATHERINE CHWOROWSKY <sup>4,5</sup> GOURAV KHULLAR (गौरव खल्लर) <sup>6,7,8</sup> KELCEY DAVIS <sup>9,‡</sup>  
STEVEN L. FINKELSTEIN <sup>4,5</sup> JANE R. RIGBY <sup>2</sup> GUILLERMO BARRO <sup>10</sup> NIKKO J. CLERI <sup>11,12,13</sup>  
DALE KOCEVSKI <sup>14</sup> JACQUELINE ANTWI-DANSO <sup>15,§</sup> MIC BAGLEY <sup>2</sup> DANIELLE A. BERG <sup>4,5</sup>  
VOLKER BROMM <sup>4,5</sup> OSCAR CHAVEZ ORTIZ <sup>4,5</sup> JOHN CHISHOLM <sup>4,5</sup> SADIE C. COFFIN <sup>16</sup>  
M. C. COOPER <sup>17</sup> OLIVIA COOPER <sup>18,¶</sup> ISA G. COX <sup>16</sup> MARK DICKINSON <sup>19</sup> HARRY FERGUSON <sup>3</sup>  
MAXIMILIEN FRANCO <sup>20</sup> JONATHAN P. GARDNER <sup>21</sup> ANANYA GANAPATHY <sup>22</sup> NORMAN GROGIN <sup>3</sup>  
MICHAELA HIRSCHMANN <sup>23</sup> MARC HUERTAS-COMPANY <sup>24,25,26,27</sup> INTAE JUNG <sup>3</sup> JEHYAN S. KARTALTEPE <sup>16</sup>  
ANTON M. KOEKEMOER <sup>3</sup> RAY A. LUCAS <sup>3</sup> ELIZABETH MCGRATH <sup>14</sup> ALEXA M. MORALES <sup>4,5,‡</sup>  
GRACE M. OLIVIER <sup>28</sup> CASEY PAPOVICH <sup>29,30</sup> PABLO G. PÉREZ-GONZÁLEZ <sup>31</sup> NOR PIRZKAL <sup>3</sup>  
RACHEL S. SOMERVILLE <sup>32</sup> ANTHONY J. TAYLOR <sup>4,5</sup> JONATHAN R. TRUMP <sup>9</sup> BRITTANY VANDERHOOF <sup>3</sup>  
BENJAMIN WEINER <sup>33</sup> BRIAN WELCH <sup>34</sup> L. Y. AARON YUNG <sup>3,†</sup> AND JORGE A. ZAVALA <sup>35</sup>

THE THRILS COLLABORATION

<sup>1</sup>Authors contributed equally to this work.

<sup>2</sup>Astrophysics Science Division, Code 660, NASA Goddard Space Flight Center, 8800 Greenbelt Rd., Greenbelt, MD 20771, USA

<sup>3</sup>Space Telescope Science Institute, 3700 San Martin Drive, Baltimore, MD 21218, USA

<sup>4</sup>Department of Astronomy, The University of Texas at Austin, Austin, TX 78712

<sup>5</sup>Cosmic Frontier Center, The University of Texas at Austin, Austin, TX 78712

<sup>6</sup>Department of Astronomy, University of Washington, Physics-Astronomy Building, Box 351580, Seattle, WA 98195-1700, USA

<sup>7</sup>Institute for Data-Intensive Research in Astrophysics and Cosmology (DiRAC), University of Washington, Physics-Astronomy Building, Box 351580, Seattle, WA 98195-1700, USA

<sup>8</sup>eScience Institute, University of Washington, Physics-Astronomy Building, Box 351580, Seattle, WA 98195-1700, USA

<sup>9</sup>Department of Physics, 196A Auditorium Road, Unit 3046, University of Connecticut, Storrs, CT 06269, USA

<sup>10</sup>University of the Pacific, Stockton, CA 90340 USA

<sup>11</sup>Department of Astronomy and Astrophysics, The Pennsylvania State University, University Park, PA 16802, USA

<sup>12</sup>Institute for Computational & Data Sciences, The Pennsylvania State University, University Park, PA 16802, USA

<sup>13</sup>Institute for Gravitation and the Cosmos, The Pennsylvania State University, University Park, PA 16802, USA

<sup>14</sup>Department of Physics and Astronomy, Colby College, Waterville, ME 04901, USA

<sup>15</sup>Department of Astronomy & Astrophysics, University of Toronto, Toronto, Ontario M5S 3H4, Canada

<sup>16</sup>Laboratory for Multiwavelength Astrophysics, School of Physics and Astronomy, Rochester Institute of Technology, 84 Lomb Memorial Drive, Rochester, NY 14623, USA

<sup>17</sup>Department of Physics & Astronomy, University of California, Irvine, Irvine, CA 92697, USA

<sup>18</sup>Department for Astrophysical & Planetary Science, University of Colorado, Boulder, CO 80309, USA

<sup>19</sup>NSF NOIRLab, 950 N. Cherry Ave., Tucson, AZ 85719, USA

<sup>20</sup>CEA, Université Paris-Saclay, Université Paris Cité, CNRS, AIM, 91191, Gif-sur-Yvette, France

<sup>21</sup>Sciences and Exploration Directorate, NASA Goddard Space Flight Center, 8800 Greenbelt Rd, Greenbelt, MD 20771, USA

<sup>22</sup>Department of Physics & Astronomy, Johns Hopkins University, Baltimore, MD 21218, USA

<sup>23</sup>Institute of Physics, Lab for galaxy evolution, EPFL, Observatoire de Sauverny, Chemin Pegasi 51, 1290 Versoix, Switzerland

<sup>24</sup>Instituto de Astrofísica de Canarias (IAC), La Laguna, E-38205, Spain

<sup>25</sup>Universidad de La Laguna. Avda. Astrofísico Fco. Sanchez, La Laguna, Tenerife, Spain

<sup>26</sup>Observatoire de Paris, LERMA, PSL University, 61 avenue de l'Observatoire, F-75014 Paris, France

<sup>27</sup>Université Paris-Cité, 5 Rue Thomas Mann, 75014 Paris, France

<sup>28</sup>The Observatories of the Carnegie Institution for Science, 813 Santa Barbara Street, Pasadena, CA 91101, USA

<sup>29</sup>Department of Physics and Astronomy, Texas A&M University, College Station, TX, 77843-4242 USA

<sup>30</sup>George P. and Cynthia Woods Mitchell Institute for Fundamental Physics and Astronomy,

Texas A&M University, College Station, TX, 77843-4242 USA

<sup>31</sup>Centro de Astrobiología (CAB), CSIC-INTA, Ctra. de Ajalvir km 4, Torrejón de Ardoz, E-28850, Madrid, Spain

<sup>32</sup>Center for Computational Astrophysics, Flatiron Institute, 162 5th Ave, New York, NY 10010, USA

<sup>33</sup>MMT/Steward Observatory, University of Arizona, 933 N. Cherry Ave., Tucson, AZ 85721, USA

<sup>34</sup>International Space Science Institute, Hallerstrasse 6, 3012 Bern, Switzerland

<sup>35</sup>University of Massachusetts Amherst, 710 North Pleasant Street, Amherst, MA 01003-9305, USA

- \* NASA Postdoctoral Fellow
- † Giacconi Postdoctoral Fellow
- ‡ NSF Graduate Research Fellow
- § Dunlap Fellow
- ¶ NSF Postdoctoral Research Fellow